ERJ Express. Published on December 21, 2018 as doi: 10.1183/13993003.00840-2018

EUROPEAN RESPIRATORY *journal*

FLAGSHIP SCIENTIFIC JOURNAL OF ERS

Early View

Original article

Fibrillin-2 is a key mediator of smooth muscle extracellular matrix homeostasis during mouse tracheal tubulogenesis

Wenguang Yin, Hyun-Taek Kim, ShengPeng Wang, Felix Gunawan, Rui Li, Carmen Buettner, Beate Grohmann, Gerhard Sengle, Debora Sinner, Stefan Offermanns, Didier Y.R. Stainier

Please cite this article as: Yin W, Kim H-T, Wang S, *et al*. Fibrillin-2 is a key mediator of smooth muscle extracellular matrix homeostasis during mouse tracheal tubulogenesis. *Eur Respir J* 2018; in press (https://doi.org/10.1183/13993003.00840-2018).

This manuscript has recently been accepted for publication in the *European Respiratory Journal*. It is published here in its accepted form prior to copyediting and typesetting by our production team. After these production processes are complete and the authors have approved the resulting proofs, the article will move to the latest issue of the ERJ online.

Copyright ©ERS 2018

Copyright 2018 by the European Respiratory Society.

Fibrillin-2 is a key mediator of smooth muscle extracellular matrix homeostasis during mouse tracheal tubulogenesis

Wenguang Yin[1*], Hyun-Taek Kim[1], ShengPeng Wang[2, 3], Felix Gunawan[1], Rui Li[2], Carmen Buettner[1], Beate Grohmann[1], Gerhard Sengle[4, 5], Debora Sinner[6], Stefan Offermanns[2, 7] and Didier Y.R. Stainier[1*]

Affiliations:

[1]Max Planck Institute for Heart and Lung Research, Department of Developmental Genetics, Bad Nauheim, Germany. [2]Max Planck Institute for Heart and Lung Research, Department of Pharmacology, Bad Nauheim, Germany. [3]Cardiovascular Research Center, School of Basic Medical Sciences, Xi'an Jiaotong University, Xi"an, China. [4]Center for Biochemistry, Medical Faculty, University of Cologne, Cologne, Germany. [5]Center for Molecular Medicine Cologne (CMMC), Cologne, Germany. [6]Division of Neonatology and Pulmonary Biology, CCHMC, University of Cincinnati, College of Medicine Cincinnati, OH, United States of America. [7]Center for Molecular Medicine, Goethe University, Frankfurt, Germany.

Correspondence:

Wenguang Yin, Department of Developmental Genetics, Max Planck Institute for Heart and Lung Research, Ludwigstrasse 43, 61231 Bad Nauheim, Germany. E-mail: Wenguang.Yin@mpi-bn.mpg.de
Didier Y.R. Stainier, Department of Developmental Genetics, Max Planck Institute for Heart and Lung Research, Ludwigstrasse 43, 61231 Bad Nauheim, Germany. E-mail: Didier.Stainier@mpi-bn.mpg.de

Abstract

Epithelial tubes, comprised of polarized epithelial cells around a lumen, are crucial for organ function. However, the molecular mechanisms underlying tube formation remain largely unknown. Here, we report on the function of Fibrillin-2 (FBN2), an extracellular matrix (ECM) glycoprotein, as a critical regulator of tracheal tube formation.

We performed a large-scale forward genetic screen in mouse to identify regulators of respiratory organ development and disease. We identified *Fbn2* mutants which exhibit shorter and narrowed tracheas as well as defects in tracheal smooth muscle (SM) cell alignment and polarity. We found that FBN2 is essential for elastic fiber formation and Fibronectin accumulation around tracheal SM cells. These processes appear to be regulated at least in part through inhibition of p38-mediated upregulation of matrix metalloproteinases (MMPs), as pharmacological decrease of p38 phosphorylation or MMP activity partially attenuated the *Fbn2* mutant tracheal phenotypes. Analysis of human tracheal tissues indicates that a decrease in ECM proteins, including FBN2 and Fibronectin, is associated with tracheomalacia.

Our findings provide novel insights into the role of ECM homeostasis in mesenchymal cell polarization during tracheal tubulogenesis.

Introduction

Smooth muscle (SM) cells surround epithelial and endothelial tubes in a number of organ systems, including the digestive tract, exocrine glands, lungs, kidneys and vasculature [1, 2]. Recent data indicate that SM cells are required for tubulogenesis in lungs, gut and blood vessels [3-5]. The trachea is a stereotypical epithelial tube that is dorsally surrounded by SM which functions to provide elasticity and control tracheal contraction [6]. The tracheal epithelium originates from ventral foregut endoderm and is specified between E8.25 and E9.0, followed by separation from the dorsal esophagus after E9.5 [7]. The tracheal SM and cartilage originate from the surrounding splanchnic mesoderm. SM cells differentiate at E11.5 [6], while cartilage development initiates as early as E9 [8], showing condensation by E13.5 [9, 10] and differentiation from E13.5 to E15.5 [11]. Tracheal epithelial cells initiate their differentiation after the establishment of SM and cartilage [12-15]. In humans, tracheal tube formation defects have been reported to cause tracheostenosis or tracheomalacia, which are characterized by a narrowing of the tracheal lumen or a deficiency of the supporting cartilage, respectively, and may lead to respiratory distress and death [16, 17]. Studies on the cellular and molecular mechanisms underlying tracheal tubulogenesis have mostly focused on the role of epithelial cells [18, 19] as well as the complex signaling between the epithelium and mesenchyme [9, 20, 21]. However, the roles of SM and cartilage during tracheal tube formation remain poorly understood.

Another poorly understood aspect of tube development is the role of the extracellular matrix (ECM) secreted by SM cells and chondrocytes. Recent data indicate that ECM cues control tube formation by mediating epithelial cell polarization [22, 23] and rearrangement [24], or orienting intercellular tension [25]. Notably, before our study, the role

of the ECM in SM cell alignment and polarity during tracheal tubulogenesis had not been addressed.

Materials and Methods

Experimental animals

Thirty C57BL/6J male mice treated with a 3 X 100 mg/kg dose of ENU [26] were obtained from Dr. Monica Justice (Baylor College of Medicine, Houston, TX). After a period of 10 weeks for the recovery of fertility, the mutagenized G0 males were crossed with C57BL/6J female mice. G1 males were outcrossed with C57BL/6J females to generate G2 females. Four G2 females were backcrossed to their G1 father, and the resulting G3 P0 pups were subject to tracheal and lung dissection and analysis. All breeding colonies were maintained under 12-hour light and 12-hour dark cycle. All mouse husbandry was performed under standard conditions in accordance with institutional (MPG) and local ethics committee (Regierungspräsidium Darmstadt, Hessen, Germany). All animal experiments were done in compliance with ethical guidelines and approved protocols.

Whole-exome sequencing analysis and genotyping

Genomic DNA isolated from two WT and two mutant mice, using a standard protocol was captured using Agilent SureSelect Mouse All Exon kit V1, and sequenced using Illumina HiSeq 2000 with minimum average 50x target sequence coverage (BGI-Hong Kong). Sequence reads were aligned to the C57BL/6J mouse reference genome (mm10) and analysed using CLCBio Genomic Workbench and GATK software. To minimize false negatives, variant calls were set at 5x minimum coverage and ≥20% alternate reads. Sequence variants were annotated to SNPs from dbSNP (version 142) and filtered against dbSNP128. For genotyping *Fbn2*$^{T2547A/T2547A}$ mice, primers Fwd (5‟-TCCAGTCATGTCGAGGGCTA-3‟) and Rev (5‟-CCAGCTTCTGCTCTTCTGCT -3‟) were used to generate a ~420 bp PCR amplicon. PCR products were sequenced using the primer Fwd (5‟-TCCAGTCATGTCGAGGGCTA-3‟) and mutations were analyzed using Biosystems Sequence Scanner Software v2.0. *Fbn2* null mice have been previously described [27]. For genotyping *Fbn2* null mice, PCR was performed as previously described [28].

Alcian blue staining of cartilage

For wholemount staining of tracheal cartilage, dissected tracheas were fixed in 95% ethanol for 12 hours followed by overnight staining with 0.03% alcian blue dissolved in 80% ethanol and 20% acetic acid. Samples were cleared in 2% KOH.

Wholemount staining of the limbs

To perform wholemount staining of E13.5 forelimbs and hindlimbs [29], samples were incubated in 70% ethanol overnight at 4°C, in 95% ethanol for 1 hour and in acetone overnight at room temperature. Samples were then stained in 0.03% alcian blue overnight, cleared by 1% KOH for 12 hours and incubated in 50% glycerol:50% 1% KOH solution for 48 hours at room temperature to make tissues transparent. To perform wholemount staining

of P6 forelimbs and hindlimbs, samples were immersed in hot water for 30 seconds at 65°C to remove all skin, incubated in 95% ethanol overnight and placed in acetone for 12 hours at room temperature. Samples were stained in 0.03% alcian blue overnight, washed twice in 70% ethanol and incubated in 95% ethanol overnight. Samples were pre-cleared in 1% KOH for 1 hour and incubated in 0.005% alizarin red for 2 hours at room temperature. Samples were kept in 50% glycerol:50% 1% KOH solution for imaging.

Primary culture of mouse tracheal chondrocytes

Tracheas were isolated from E14.5 embryos. To isolate chondrocytes [30], each trachea was incubated in 10 ml of collagenase D solution at 0.5 mg/ml for 12 hours at 37°C. Samples were then passed through 2-ml Pasteur pipettes to disperse any cell aggregates. The cell suspension was filtered through a sterile 40 μm cell strainer over a 50-ml tube and centrifuged for 10 minutes at 400 g at room temperature. The pellet was washed in 2 ml PBS. Chondrocytes from each trachea were seeded on a 24-well cell culture plate and cultured in DMEM/F-12 medium containing 10% FBS at 37°C in a 5% CO_2 incubator for 9 days.

Alcian blue staining of cultured tracheal chondrocytes

Mouse tracheal chondrocytes in primary cultures were washed twice in PBS and fixed in 1 ml of 4% glutaraldehyde for 15 minutes at room temperature. Samples were washed twice in 2 ml of 0.1 M HCl followed by staining with 1% alcian blue dissolved in 0.1 M HCl for 30 minutes. After three washes in 2 ml of 0.1 M HCl, samples were dried and rehydrated with 1 ml of 0.1 M HCl.

Quantification of relative alcian blue area

Alcian blue area was measured using ImageJ. Relative alcian blue area was calculated by the ratio of alcian blue area to total cell area, and WT was assigned as 1.

Tracheal tube length measurements

Tracheal tube length was determined by measuring the distance between the first and last tracheal cartilage rings.

Respiratory rate measurements

Respiratory rates were determined by measuring the number of breaths per minute. Unexpectedly, $Fbn2^{T2547A/T2547A}$ mice exhibit WT-like respiratory rates at rest. It is possible that $Fbn2^{T2547A/T2547A}$ mice would display difficulties in breathing during high-intensity exercise.

Wholemount immunostaining

Tracheas were isolated from E12.5 to E16.5 embryos, and P0 and P60 mice. Tracheas were then fixed in 4% paraformaldehyde overnight at 4°C and washed three times in PBS for 1 hour each. Samples were incubated in 5% FBS/PBS/0.5% Triton X-100/3% BSA for 12

hours and then in primary antibodies overnight at 4°C. After six washes in 0.5% Triton X-100/PBS for 1 hour each, samples were incubated in secondary antibodies overnight at 4°C. Samples were washed six times in 0.5% Triton X-100/PBS for 1 hour each and mounted for imaging. To visualize smooth muscle (SM) cells and chondroblasts, tracheas were stained for αSMA and SOX9, respectively. To visualize the Golgi apparatus, tracheas were stained for GM130. To visualize elastic fibers and Fibronectin (FN), tracheas were stained for Tropoelastin and FN.

Quantification of short elastic fibers

The number of short elastic fibers was counted per field of view using ImageJ.

Immunostaining of cryosections

Tracheas and lungs were dissected in PBS, fixed in 4% paraformaldehyde overnight at 4°C, incubated in 10% sucrose and 30% sucrose for 24 hours each at 4°C, mounted in OCT embedding compound, and sectioned at 10 µm thickness. Immunostaining was carried out using standard protocols. Immunostaining for phospho-p38 and αSMA was carried out with WT and mutant trachea sections on the same slide.

Quantification of SFTPC$^+$ cell ratio

SFTPC$^+$ and total cell number was counted per field of view using ImageJ. SFTPC$^+$ cell ratio was calculated as SFTPC$^+$ cells/total cells.

Quantification of the mitotic angle

The epithelial plane is marked by a white dashed line, and the axis of mitosis by a green dashed line. The angle between these two lines represents the mitotic angle and was measured using ImageJ.

In situ hybridization of cryosections

Tracheas were dissected in PBS, fixed in 4% paraformaldehyde overnight at 4°C, mounted in OCT embedding compound, and sectioned at 10 µm thickness. To perform *in situ* hybridization [31], cryosections were permeabilized in 5 µg/ml proteinase K (Roche, REF 04693159001) for 15 minutes at room temperature, followed by acetylation for 2 minutes and pre-incubation in hybridization buffer for 3 hours at 70°C, incubated with DIG-labeled RNA antisense probes overnight at 70°C, washed, incubated with alkaline phosphatase-conjugated anti-digoxigenin antibody (Roche) overnight at 4°C, washed, and the signal was detected with NBT-BCIP staining solution (Roche).

Western blotting

Isolated P7 tracheas were lysed using RIPA buffer (Cell Signaling, 9806) supplemented with protease and phosphatase inhibitors (Cell Signaling, 5872). Lysates were centrifuged at 10,000 g for 10 minutes, subjected to SDS-PAGE and transferred to nitrocellulose membranes. Membranes were probed with primary and HRP-conjugated secondary

antibodies (Cell Signaling Technology) and were developed using the ECL detection system (Pierce).

Gelatin zymography

Isolated P7 tracheas were put in a lysis buffer (0.025 M Tris–HCl, pH 7.5, 0.1 M NaCl, and 1% v/v Nonidet P-40 (NP-40) supplemented with a Protease Inhibitor Cocktail-EDTA Free (Roche, REF 04693159001). Lysates were centrifuged at 16,000 g for 10 minutes at 4°C. The supernatant was collected and protein concentration measured. Equal amounts of protein were loaded per lane of gelatin zymography gels. The gel was then incubated in renaturing solution for 30 minutes at room temperature, washed twice in 300 ml of dH_2O, incubated in developing buffer for 30 minutes and incubated in fresh developing buffer for another 16 hours. After staining with Coomassie Blue, the gel was destained for examining gelatinolytic activity.

Quantification of western blot signals

Fibronectin, active MMP2, MMP9, total p38, phospho-p38, and GAPDH levels were quantified using ImageJ. Fibronectin, active MMP2, MMP9, total p38 and phospho-p38 levels were normalized to the values yielded by GAPDH. Phospho-p38 fold change was calculated by the ratio of phospho-p38/p38 and WT was assigned to 1.

Reverse transcription quantitative PCR (RT–qPCR)

Total RNA was extracted using a miRNeasy Mini Kit (Qiagen). cDNA was synthesized using the Maxima First Strand cDNA Synthesis Kit (ThermoFisher Scientific), according to manufacturer‟s instructions. Quantitative real-time PCR was performed using Eco Real-Time PCR System (Illumina) and Maxima SYBR Green/Fluorescein qPCR Master Mix (ThermoFisher Scientific). Mean Ct values are shown in Supplementary table 1. *Actb* was used as a reference gene. The following primers were used: *Actb* forward 5‟-CGGCCAGGTCATCACTATTGGCAAC-3‟ and *Actb* reverse 5‟-GCCACAGGATTCCATACCCAAGAAG-3‟; *Atf2* forward 5‟-ACTCCAACGCCAACAAGATTC-3‟ and *Atf2* reverse 5‟-TCTACAACAGAAGGCTCCTCAAT-3‟; *Fos* forward 5‟-GGGGACAGCCTTTCCTA-3‟ and *Fos* reverse 5‟-CTGTCACCGTGGGGATAAAG-3‟; *Jun* forward 5‟-ACGACCTTCTACGACGATGC-3‟ and *Jun* reverse 5‟-CCAGGTTCAAGGTCATGCTC-3‟; *Fbn1* forward 5‟-ACGGCTTTACTGGACCCCA-3‟ and *Fbn1* reverse 5‟-ACATCTGGTTGCTTACCACAG-3‟; *Fbn2* forward 5‟-CCACTCCTATTGCTGCCCAG-3‟ and *Fbn2* reverse 5‟-TTGGGGCGGGAACAGAATC-3‟; *Fibronectin* forward 5‟-GGCATCGGGGAGTGGCACTG-3‟ and *Fibronectin* reverse 5‟-ATTGGGCTGGCTGGGGGTCT-3‟; *Fgf10* forward 5‟-CGGGACCAAGAATGAAGACT-3‟ and *Fgf10* reverse 5‟-AGTTGCTGTTGATGGCTTTG-3‟; *Hspb1* forward 5‟-ATCCCCTGAGGGCACACTTA-3‟ and *Hspb1* reverse 5‟-GGAATGGTGATCTCCGCTGAC-3‟; *Mmp2* forward 5‟-ACCCAGATGTGGCCAACTAC-3‟ and *Mmp2* reverse 5‟-TACTTTTAAGGCCCGAGCAA-3‟; *Mmp9* forward 5‟-

TAAGGACGGCAAATTTGGTT-3‟ and *Mmp9* reverse 5‟-CTTTAGTGGTGCAGGCAGAG-3‟; *Nfkb1* forward 5‟-CGTAACAGCAGGACCCAAGG-3‟ and *Nfkb1* reverse 5‟-CTGTCATCCGTGCTTCCAGT-3‟; *Nfkb2* forward 5‟-TTCAGAGTTGGGAGTGTGCG-3‟ and *Nfkb2* reverse 5‟-TGGTTACATGCAGGACACCC-3‟; *Rela* forward 5‟-CGGATTCCGGGCAGTGAC-3‟ and *Rela* reverse 5‟-GAGGGGAAACAGATCGTCCA-3‟.

GM6001 and SB203580 injections; in vitro treatments with SB203580 and methylamine hydrochloride

GM6001 and SB203580 were dissolved in 100% DMSO (stock) and diluted with 0.9% saline. Methylamine hydrochloride was dissolved in ddH_2O (stock). Plugged C57BL6/J females were treated daily with intraperitoneal injections of GM6001 (50 mg/kg) or SB203580 (1 μM/kg) between E12.5-E14.5. The vehicle used for control injections was DMSO in 0.9% saline solution. E15.5 embryos were harvested for trachea isolation. For *in vitro* treatment with SB203580, isolated tracheas were cultured in DMEM/F-12 medium containing 0.1% DMSO or 1 μM SB203580 at 37°C in a 5% CO_2 incubator for 20 hours. For *in vitro* treatment with methylamine hydrochloride, isolated tracheas were cultured in DMEM/F-12 medium containing 1.5% ddH_2O or 30 μM methylamine hydrochloride at 37 °C in a 5% CO_2 incubator for 25 hours.

Tracheal phenotype analysis after treatments

Evaluation of tracheal tube length, SM orientation, elastic fiber formation and FN accumulation after GM6001 or SB203580 injection or treatment was done prior to genotyping.

Antibodies

The following antibodies were used: Mouse anti-αSMA-Cy3 (1:1000, Sigma-Aldrich, C6198); Rat anti-CDH1 (1:500, Santa Cruz, sc-59778); Rabbit anti-SOX9 (1:400, Millipore, AB5535); Goat anti-SOX9 (1:200, R&D systems, AF3075); Sheep anti-GM130 (1:50, R&D systems, AF8199); Rabbit anti-Ki67 (1:400, Cell Signaling Technologies, #9027); Mouse anti-PCNA (1:400, Santa Cruz, sc-56); Rabbit anti-Cleaved Caspase-3 (1:600, Cell Signaling Technologies, #9661); Rabbit anti-Phospho-p38 (1:100 for immunostaining and 1:1000 for western blots, Cell Signaling Technologies, #9215); Rabbit anti-p38 (1:1000, Cell Signaling Technologies, #9212); Rabbit anti-MMP-9 (1:1000, Millipore, AB19016); Rabbit-MMP-2 (1:1000, Millipore, AB19015); Rabbit anti-FBN2 (1:5000 for immunostaining and 1:2000 for western blots); Guinea pig anti-FBN2 (1:500); Rabbit anti-Tropoelastin (1:1000 for immunostaining and 1:1000 for western blots, Abcam, ab21600); Sheep anti-Fibronectin (1:1000, Novus Biologicals, AF1918); Rabbit anti-Fibronectin (1:500 for immunostaining and 1:1000 for western blots, Sigma, F3648); Goat anti-Aggrecan (1:200, R&D Systems, AF1220); Rabbit anti-COL2A1 (1:50, Millipore, AB761); Rabbit anti-PH3 (1:400, Millipore, 06-570); Rat anti-RAGE (1:400, R&D systems, MAB1179); Rat anti-PECAM (1:200, BD Biosciences, 553370); Goat anti-CC10 (1:200, Santa Cruz, T-18); Rabbit anti-SFTPC (1:400, Millipore, AB3786); Mouse anti-acetylated alpha-tubulin (1:2000, Sigma, T-7451); Goat

anti-Vimentin (1:200, Santa Cruz, C-20); and Rabbit anti-GAPDH (1:3000, Cell Signaling Technologies, #2118). Polyclonal rabbit and guinea pig anti-Fibrillin-2 antisera were raised against the N-terminal recombinant human Fibrillin-2 polypeptide rF86 (Gln^{29}-Asp^{535}) in 293 Epstein-Barr virus nuclear antigen (EBNA) cells [32]. Antisera were purified before use by affinity chromatography on a column with antigen coupled to cyanogen bromide-activated Sepharose (GE Healthcare).

Explant culture of mouse embryonic tracheas and lungs, and in vitro treatment with protease

Tracheas and lungs were isolated from E13.5 embryos and cultured using an established protocol [33]. For *in vitro* treatment with elastase or collagenase type II, isolated tracheas and lungs were cultured in DMEM/F-12 medium or DMEM/F-12 medium containing 2 mU/ml elastase (Worthington Biochemical Corporation, LS002290) or DMEM/F-12 medium containing 2 mU/ml collagenase type II (Gibco, 9001-12-1) at 37°C in a 5% CO_2 incubator for 28 hours.

Ex vivo trachea physiology

2 mm sections of tracheas were isolated from P1 pups and kept in Krebs solution (119 mM NaCl, 4.7 mM KCl, 2.5 mM $CaCl_2$, 1.17 mM $MgSO_4$, 20 mM $NaHCO_3$, 1.18 mM KH_2PO_4, 0.027 mM EDTA, 11 mM glucose) aerated with carbogen at 37°C. Tracheal rings were mounted in a wire-myograph system (610-M, Danish Myo Technology) and a resting tension of 2 mN was applied for each ring as a baseline. Contractile responses were determined by cumulative administration of indicated acetylcholine concentrations. For spontaneous contraction analysis of fetal tracheas, E13.5 tracheas were isolated and kept in PBS for time-lapse imaging for 10 minutes every 1 second with a Zeiss LSM 800 inverted laser scanning confocal microscope. The amplitude of spontaneous contractions was defined as „1 - the ratio of tracheal SM minimum width after contraction to maximum width after relaxation".

Human tracheomalacia samples

Paraffin sections of deidentified human tracheomalacia samples and healthy tracheal tissues (controls) were provided by Cincinnati Children"s Hospital Medical Center Biobank Core facility. The clinical diagnosis of tracheomalacia was confirmed by histological analysis. The study protocol and tissue usage were approved by the institutional ethics committee. Written informed consent was obtained from all patients" families prior to collection of samples by "Better Outcomes for Children" biorepository.

Imaging

Imaging of wholemount tracheas, lungs and limbs, and trachea and lung sections was performed using a Nikon SMZ25, Nikon 90i, Zeiss Axio Imager.A2, Zeiss LSM 800 inverted or 880 upright laser scanning confocal microscope. Quantification of tube length, distance between the C-shaped rings, ring width, SM area, SM cell orientation and nuclear aspect ratio (NAR), Golgi apparatus position relative to the nucleus, elastic fiber orientation, short elastic fibers, immunofluorescence intensity, cell number and mean linear intercept was performed

using ImageJ (http://rsbweb.nih.gov/ij/). In straight and bent tracheas, tube length was measured by drawing a freehand line along the outer edge of the trachea in an anterior-posterior direction in ImageJ.

Statistical analysis

Statistical analyses were performed using GraphPad software. P values were calculated by Student‟s *t*-test (*****P<0.05; ******P<0.01; *******P<0.001; NS, not significant).

Results

Fbn2$^{T2547A/T2547A}$ mice exhibit tracheal tube formation defects

To identify novel loci regulating mouse respiratory organ formation, we conducted a large-scale forward genetic screen using ethylnitrosourea (ENU) mutagenesis. One of the recessive mutants identified in this screen exhibits lower body weight (figure 1a, b and supplementary figure S1A, B), decreased nose to anus length (supplementary figure S1A, C), a shortened trachea (figure 1c, d and supplementary figure S1D), fewer cartilage rings (figure 1c, e), a narrowed tracheal lumen (figure 1f, g), but WT-like respiratory rate (supplementary figure S1E). These mutant animals are born in the expected Mendelian ratio, indicating that this mutation does not cause embryonic lethality. To identify the phenotype-causing mutation, we performed whole-exome sequencing of G4 genomic DNA samples and identified *Fbn2*, which encodes an ECM glycoprotein, as a candidate gene (figure 1h). Next, we carried out genetic linkage analysis by genotyping 189 G4, G5 and G6 mutant animals and found complete linkage between the tracheal phenotypes and the *Fbn2$^{T2547A/T2547A}$* allele (figure 1i). The identified allele carries a nonsense mutation (c.T2547A) at a highly conserved amino acid (figure 1j), which is predicted to cause a truncated protein with 848 amino acids (p.C849X) (figure 1k). We then carried out a complementation test by crossing mice carrying the ENU-induced *Fbn2* allele (*Fbn2$^{T2547A/+}$*) with mice carrying a *Fbn2* deletion allele [27], and found that complementation did not occur in the *Fbn2$^{-/T2547A}$* double heterozygous animals (figure 1l), indicating that loss of *Fbn2* function is likely responsible for the observed tracheal phenotypes in the *Fbn2$^{T2547A/T2547A}$* mice. To further test the role of *Fbn2* in tracheal development, we analyzed tracheal formation in *Fbn2$^{-/-}$* mice. *Fbn2$^{-/-}$* mice exhibit a shortened trachea with fewer and fractured cartilage rings (supplementary figure S2A-C) and disorganized SM (supplementary figure S2C, D). *Fbn2$^{-/-}$* mice have been reported to exhibit skeletal limb abnormalities [27]. We thus examined limb formation in *Fbn2$^{T2547A/T2547A}$* mice. Interestingly, *Fbn2$^{T2547A/T2547A}$* mice exhibit bilateral syndactyly of the central digits in the hindlimbs as early as E13.5 (supplementary figure S3A), and until adulthood (supplementary figure S3B, C). However, we observed no significant phenotype in *Fbn2$^{T2547A/T2547A}$* forelimbs (supplementary figure S3D-F). To test for a possible role of *Fbn2* in lung development, we analyzed the intrapulmonary airways and the lungs. *Fbn2$^{T2547A/T2547A}$* mice exhibit cartilage formation defects in the intrapulmonary airways (supplementary figure S4A-D). However, we observed no significant phenotype in lung branching morphogenesis (supplementary figure S5A, B), alveologenesis (supplementary figure S5C, D), or lung cell differentiation (supplementary figure S6A-I) in *Fbn2$^{T2547A/T2547A}$*

animals. In addition, we examined tracheal tube formation and limb patterning in *Fbn2*$^{T2547A/+}$ animals. *Fbn2*$^{T2547A/+}$ mice exhibit WT-like tracheal length (supplementary figure S7A, B), cartilage formation (supplementary figure S7A, C), SM cell orientation (supplementary figure S7D, E) and limb patterning (supplementary figure S7F), indicating haplosufficiency of *Fbn2*. Altogether, these findings strongly suggest that *Fbn2* regulates tracheal tube formation.

FBN2 surrounds tracheal SM cells and chondroblasts

To examine the spatiotemporal expression patterns of FBN2 in the developing mouse trachea, we performed immunostaining during embryonic and postnatal stages using a polyclonal antibody raised against amino acids 29-535. FBN2 appears to localize around the tracheal mesenchyme including the SM cells and chondroblasts as early as E12.5 (figure 2a). Interestingly, FBN2 expression levels appear gradually reduced around chondroblasts during chondrocyte differentiation from E14.5 to E18.5 (figure 2b), such that FBN2 immunostaining was barely detectable around tracheal chondrocytes at postnatal stages (figure 2b). We then examined *Fbn2* mRNA expression in developing tracheas. In E14.5 tracheas, *Fbn2* appeared to be exclusively expressed in mesenchymal cells, including the chondroblasts (supplementary figure S8A). However, at E16.5, *Fbn2* mRNA levels appeared to be reduced in tracheal chondrocytes (supplementary figure S8B) and were mainly detected in other mesenchymal cells, including tracheal SM cells (supplementary figure S8C). These data indicate that FBN2 is required for tracheal SM cell and chondrocyte development at early embryonic stages. Next, we investigated *Fbn2*$^{T2547A/T2547A}$ mRNA and protein: mutant mRNA levels were significantly reduced compared to WT (figure 2c and supplementary table 1), suggesting mRNA decay. No FBN2 immunoblot (figure 2d) or immunostaining (figure 2e) signal was observed in the mutant animals, indicating that the truncated *Fbn2*$^{T2547A/T2547A}$ protein is not synthesized or is highly unstable. These results indicate that the *Fbn2*$^{T2547A/T2547A}$ mutation leads to a reduction of FBN2 at both the mRNA and protein levels.

Fbn2$^{T2547A/T2547A}$ *mice display defects in tracheal elongation, cartilage ring formation and SM organization*

To examine the formation of the trachea in more detail, we performed a systematic analysis of tracheal tube development. *Fbn2*$^{T2547A/T2547A}$ mice display no obvious differences in tracheal tube length compared to WT siblings at E12.5 (figure 3a, c). However, starting at E13.5, we observed that *Fbn2*$^{T2547A/T2547A}$ tracheas were shorter than their WT counterparts (figure 3a, c), and this phenotype became more pronounced at postnatal stages (figure 3b, c). These results suggest that impaired tracheal tube elongation occurs after SM differentiation, which starts at E11.5 [6]. To identify alterations in tracheal architecture, we performed a structural analysis of the cartilage and SM. Cartilage formation occurs as a result of the condensation of mesenchymal cells followed by chondrogenic differentiation [34]. Starting at E13.5, chondrogenic nodules resulting from SOX9^{+} mesenchymal cell condensation were observed (figure 3d). However, *Fbn2*$^{T2547A/T2547A}$ tracheas exhibited a reduced number of C-shaped rings starting at E13.5 and until adulthood (figure 3d-f). Moreover, starting at E14.5,

an increased distance between the C-shaped rings (figure 3d, g) and a decreased ring width (figure 3d, h) were observed in *Fbn2*$^{T2547A/T2547A}$ tracheas. FBN2 levels decline progressively during chondrogenic differentiation of mouse ATDC5 cells [35], similar to what is observed in tracheal chondroblasts (figure 2b). Thus, we hypothesized that FBN2 deficiency might lead to compromised tracheal chondrocyte differentiation. To test this hypothesis, we examined expression levels of aggrecan (AGC1) and type II collagen (COL2A1), chondrocyte-specific markers [34], and observed that AGC1 (supplementary figure S9A, B) and COL2A1 (supplementary figure S9C, D) levels were significantly reduced in *Fbn2*$^{T2547A/T2547A}$ tracheas. In contrast, we did not find obvious alterations in apoptosis (supplementary figure S10A-C) or SOX9^{+} chondroblast proliferation (supplementary figure S10D, E) between WT and *Fbn2*$^{T2547A/T2547A}$ tracheas, indicating that FBN2 deficiency causes abnormal tracheal rings by inhibiting chondrocyte differentiation. We then isolated immature chondrocytes from E14.5 tracheas and cultured them for 9 days. Interestingly, *Fbn2*$^{T2547A/T2547A}$ chondrocytes exhibited reduced alcian blue staining in primary cultures (supplementary figure S11A, B), suggesting that *Fbn2* regulates cartilage formation in a cell-autonomous manner. Since altered SM morphogenesis can affect tube elongation [4, 10, 36], we analyzed tracheal SM development. SM cells, which are positioned dorsally in the trachea, displayed no obvious differences between WT and *Fbn2*$^{T2547A/T2547A}$ animals at E12.5 (figure 3i, j), indicating that FBN2 is dispensable for SM differentiation and early steps in SM morphogenesis. Disorganized SM stripes of decreased area were first observed in *Fbn2*$^{T2547A/T2547A}$ tracheas at E13.5 (figure 3i, j) and became more noticeable starting at E14.5 (figure 3i, j). In contrast, *Fbn2*$^{T2547A/T2547A}$ tracheal SM cells did not exhibit significant changes in apoptosis (supplementary figure S10A-C) or proliferation (supplementary figure S10F, G) compared to WT. Similarly, mitotic spindle orientation (supplementary figure S12A, B) and cell proliferation (supplementary figure S12C, D) in the tracheal epithelium of *Fbn2*$^{T2547A/T2547A}$ mice appeared to be unaffected compared to WT. Since *Fgf10* is expressed in tracheal SM cells and modulates airway patterning [20], we also tested *Fgf10* mRNA levels. *Fbn2*$^{T2547A/T2547A}$ tracheas exhibited no significant difference in *Fgf10* expression levels (supplementary figure S12E and supplementary table 1), indicating that *Fbn2* signals via a *Fgf10* independent pathway to regulate tracheal patterning. Collectively, these results suggest that chondrocyte differentiation and SM organization are essential for tracheal tube formation.

***Fbn2* mediates SM cell orientation and polarization**

Longitudinal SM has been reported to restrict gut tube elongation by compressing the mesenchyme and attached epithelium [4]. Our findings that FBN2 is required for SM organization led us to hypothesize that the tracheal elongation defects observed in *Fbn2*$^{T2547A/T2547A}$ mice might be due to altered SM cell alignment. Thus, we performed a systematic analysis of SM cell orientation. In WT animals, differentiated tracheal SM cells exhibit round shapes and progressively develop into spindle-shaped cells that circumferentially align the tube by E13.5 (figure 4a, b). We observed no significant differences in SM alignment between *Fbn2*$^{T2547A/T2547A}$ and WT tracheas at E12.5 (figure 4c, d). However, at E13.5, *Fbn2*$^{T2547A/T2547A}$ SM cells displayed random alignment (figure 4c, d),

and this phenotype was observed also in adult animals (figure 4c, d). This SM phenotype temporally correlates with the onset of the tracheal elongation defects in *Fbn2*$^{T2547A/T2547A}$ mice (figure 3c, d). Correct orientation of the cell body has been shown to depend on the establishment of cell polarity [37]. To better understand the polarization of SM cells, we examined the localization of the Golgi apparatus relative to the cell nucleus, using the cis-Golgi matrix marker GM130, a widely used method to determine cell polarity in various cell types [38, 39]. In WT SM cells, the GM130-labeled Golgi localizes preferentially by the long edges of the nucleus (figure 4e, f). In contrast, in *Fbn2*$^{T2547A/T2547A}$ SM cells, the Golgi exhibited random alignment (figure 4e, f). Tracheal SM cells establish polarity before E12.5, and its disruption causes altered SM architecture by E12.5 [36]. *Fbn2*$^{T2547A/T2547A}$ SM exhibited no significant differences compared to WT at E12.5 (figure 4c, d). These results indicate that *Fbn2* is dispensable for the initiation of SM cell polarity, but becomes necessary for its maintenance. Tissue contractility has been reported to drive tubulogenesis [40, 41]. Based on the findings that *Fbn2* is required for SM cell alignment and polarity, we hypothesized that a disruption in SM cell orientation might lead to compromised circumferential tracheal contraction contributing to tube elongation defects in *Fbn2* mutant mice. Interestingly, *Fbn2*$^{T2547A/T2547A}$ tracheas exhibited increased duration (figure 4g, h and supplementary movie 1) and reduced amplitude (figure 4g, i and supplementary movie 1) of spontaneous contractions compared to WT at E13.5. In addition, *Fbn2*$^{T2547A/T2547A}$ tracheas exhibited significantly reduced contractile forces compared to WT (figure 4j). These findings indicate that FBN2 is essential to maintain SM cell polarity to direct tissue architecture and contractility, ultimately driving tracheal tube elongation.

The esophagus and trachea separate from a common foregut tube at around E9.5 [42]. Thus, we sought to determine whether *Fbn2* was also required for esophageal tube formation. FBN2 is highly expressed in esophageal SM (supplementary figure S13A), but we found no significant difference in tube length between *Fbn2*$^{T2547A/T2547A}$ and WT mice (supplementary figure S13B, C). Next, we examined esophageal SM morphology. SM cells are localized in the outer layers of the esophageal wall [43] (supplementary figure S13A, D), and spindle-shaped SM cells are circumferentially aligned by E14.5 (supplementary figure S13E, F). Unlike in the trachea, we observed no obvious differences in esophageal SM organization (supplementary figure S13D) or SM cell orientation (supplementary figure S13E, F) between *Fbn2*$^{T2547A/T2547A}$ and WT mice. These data indicate that *Fbn2* is dispensable for SM development during esophageal tube formation.

***Fbn2* modulates elastic fiber formation and Fibronectin accumulation**

To investigate the molecular mechanisms underlying *Fbn2*-mediated tracheal tube formation, we examined ECM protein formation and levels. Fibrillin microfibrils are known to provide a scaffold for the deposition of Tropoelastin, which matures to Elastin and eventually to elastic fibers [44-48]. We hypothesized that *Fbn2* deficiency might lead to defects in Elastin structure. At E14.5, elastic fibers around WT SM cells were aligned parallel to the long edges of the nuclei and approximately perpendicular to the direction of tube elongation (figure 5a, b). In contrast, elastic fiber orientation in *Fbn2*$^{T2547A/T2547A}$ tracheas appeared

random, with most of them oriented at an angle oblique to the direction of tube elongation (figure 5a, b). Interestingly, short elastic fibers were also observed in *Fbn2*$^{T2547A/T2547A}$ tracheas unlike in WT (figure 5a, c). However, *Fbn2*$^{T2547A/T2547A}$ tracheas exhibited no obvious changes in Elastin protein levels (figure 5d), indicating that FBN2 is required for elastic fiber formation but not Elastin protein expression. Next, we examined elastic fibers in esophageal SM cells. There was no significant difference in elastic fiber formation between *Fbn2*$^{T2547A/T2547A}$ and WT esophagi (supplementary figure S13G-I). *Fbn1* has been reported to modulate elastic fiber formation [49-51]. However, *Fbn2* null mutants exhibit WT-like vascular SM cells and elastic fiber formation [45]. Interestingly, *Fbn1* is highly expressed in esophagi (supplementary figure S13J) and FBN1 localizes to blood vessel walls [52]. These results suggest that *Fbn1* and *Fbn2* may play redundant functions in esophageal and vascular SM morphogenesis.

Another critical ECM protein, Fibronectin (FN), has been shown to bind FBN2 [53, 54] and promote cell elongation and alignment [55, 56]. Interestingly, *Fbn2*$^{T2547A/T2547A}$ tracheas exhibited significantly decreased FN protein levels compared to WT (figure 5d-g), indicating that FN accumulation is dependent on FBN2. However, we observed no significant difference in Fn mRNA levels in *Fbn2*$^{T2547A/T2547A}$ tracheas compared to WT (figure 5h). Methylamine hydrochloride (MA), a lysosomal inhibitor, has been reported to inhibit FN degradation [57]. After treatment with MA, *Fbn2*$^{T2547A/T2547A}$ tracheas exhibited partially restored FN protein levels (figure 5i, j), indicating that FBN2 protects FN from lysosomal degradation during tracheal tube formation. To test whether FBN2 plays a role in elastic fiber formation and FN accumulation in adult mice, we examined elastic fibers and FN in adult tracheas. We found that *Fbn2*$^{T2547A/T2547A}$ P70 tracheas exhibited random elastic fiber orientation (supplementary figure S14A, B), short elastic fibers (supplementary figure S14A, C), decreased FN protein levels (supplementary figure S14D, E), but no obvious difference in Elastin protein levels (supplementary figure S14F, G) compared to WT, possibly suggesting that FBN2 is needed for ECM homeostasis in mature mice. However, to examine the adult function of *Fbn2*, it will be necessary to generate and use a floxed *Fbn2* allele. Elastin deficiency has been reported to alter the orientation of SM cells in the vessel wall [58, 59]. We thus hypothesized that disruption of elastic fibers might phenocopy the *Fbn2* deficiency-induced tracheal elongation and SM cell orientation defects. Interestingly, after treatment for 28 hours with 2 mU/ml elastase, E13.5 tracheas exhibited a significant reduction in tube length (figure 5k, l) and altered SM cell orientation (figure 5m, n) compared to controls, phenotypes that were not observed after treatment with collagenase type II (figure 5k-n). Altogether, these results suggest that FBN2-mediated ECM formation and accumulation are essential for tracheal SM cell orientation and organ elongation.

p38-dependent downregulation of Mmp expression as a mediator of Fbn2 function in tracheal development

We sought to further understand how FBN2 deficiency leads to impaired ECM formation and accumulation. The observation of short elastic fibers and FN degradation prompted us to analyze the levels of matrix metallopeptidase 2 (MMP2) and MMP9, key Elastin and

Fibronectin-cleaving enzymes [60-63]. *Fbn2*$^{T2547A/T2547A}$ tracheas exhibited significantly increased *Mmp2* and *Mmp9* mRNA levels (figure 6a and supplementary table 1) as well as increased protein levels (figure 6b, c), and activity (figure 6d, e). In contrast, *Fbn2*$^{T2547A/T2547A}$ esophagi exhibited no obvious difference in *Mmp2* mRNA levels (supplementary figure S15A and supplementary table 1), while *Mmp9* mRNA was undetectable in E14.5 WT esophagi (supplementary table 1). MMP inhibition by GM6001 [64] has been shown to reduce Elastin cleavage [65] and FN degradation [66]. We thus tested whether MMP inhibition could rescue the *Fbn2*$^{T2547A/T2547A}$ tracheal phenotypes. We administered GM6001 (50 mg/kg) intraperitoneally (IP) for 3 consecutive days from E12.5 to E14.5. Interestingly, after GM6001 injection, *Fbn2*$^{T2547A/T2547A}$ tracheas exhibited partially rescued tube elongation (figure 6f, g) and SM orientation (figure 6h, i) phenotypes, as well as partially restored elastic fiber formation (figure 6h, j, k) and FN accumulation (figure 6h, l) as assessed in a blind analysis. We aimed to find mechanisms by which *Fbn2* regulates *Mmp2* and *Mmp9* expression and thus examined the expression of *Atf2* and *Hspb1*, potential regulators of *Mmp2* expression [67], as well as *Nfkb1*, *Nfkb2*, *Rela, Jun* and *Fos*, potential regulators of *Mmp9* expression [67]. *Fbn2*$^{T2547A/T2547A}$ tracheas exhibited WT-like expression levels of these genes (supplementary figure S15B, C and supplementary table 1), indicating that *Fbn2* modulates *Mmp2 and Mmp9* mRNA levels through other pathways.

Mmps have been identified to be downstream targets of p38 MAPK signaling [68], and inhibition of the p38 MAPK signaling pathway efficiently downregulates *Mmp2* and *Mmp9* expression [68, 69]. Thus, we hypothesized that Fbn2 deficiency might lead to increased p38 MAPK activity. We observed that levels of phosphorylated p38 were greatly elevated in *Fbn2*$^{T2547A/T2547A}$ tracheas compared to WT (figure 7a, b and supplementary figure S16A, B), a phenotype that was not observed in *Fbn2*$^{T2547A/T2547A}$ esophagi (supplementary figure S16C, D). In addition, after treatment with SB203580, a small molecule that decreases p38 phosphorylation [70], *Fbn2*$^{T2547A/T2547A}$ tracheas exhibited partially restored *Mmp2* and *Mmp9* mRNA levels (figure 7c and supplementary table 1). We then administered SB203580 (1 μM/kg) intraperitoneally for 3 consecutive days from E12.5 to E14.5. Notably, after SB203580 injection, *Fbn2*$^{T2547A/T2547A}$ tracheas exhibited partially rescued tube elongation (figure 7d, e) and SM orientation (figure 7f, g) phenotypes, restored elastic fiber formation (figure 7f, h, i) as well as FN accumulation (figure 7f. j) as assessed in a blind analysis. These results indicate that an increase in p38 phosphorylation-mediated *Mmp* levels in *Fbn2*$^{T2547A/T2547A}$ tracheas partially accounts for the SM cell orientation phenotype via its action on ECM homeostasis (figure 7k).

FBN2 and Fibronectin are decreased in the tracheas of human tracheomalacia patients

Since *Fbn2*$^{T2547A/T2547A}$ mice exhibited tracheal cartilage defects, phenotypes similar to those observed in tracheomalacia patients (figure 8a), we examined FBN2 expression in tracheas from healthy controls and tracheomalacia patients (supplementary table 2). FBN2 localized to the peripheral regions of tracheal cartilage (figure 8b) and did not surround SOX9^{+} mesenchymal cells (figure 8b) in postnatal human tracheas, expression patterns similar to those observed in mice at postnatal stages (figure 2b). We observed that FBN2 levels were

significantly decreased in the cartilage regions of tracheas from tracheomalacia patients compared to healthy controls (figure 8b, c). We also examined Fibronectin expression. Fibronectin localized to the peripheral regions of tracheal cartilage (figure 8d) and did not surround $SOX9^{+}$ mesenchymal cells (figure 8d) in postnatal human tracheas, expression patterns similar to those observed in mice at postnatal stages (supplementary figure S17). Interestingly, Fibronectin levels also appeared to be reduced in the cartilage regions of tracheas from tracheomalacia patients compared to healthy controls (figure 8d, e). These results in humans are consistent with findings in mice, suggesting that a decrease in ECM proteins, including FBN2 and Fibronectin, is associated with, and may contribute to, symptoms of tracheomalacia.

Discussion

Understanding tracheal tubulogenesis is a fundamental goal in the field of pulmonary development and disease, as conditions such as primary tracheomalacia and congenital tracheal stenosis arise due to tracheal tube formation defects. Our work suggests critical roles for SM cells and chondrocytes in tracheal tube formation. Differentiated SM cells elongate in a direction perpendicular to the axis of tracheal elongation and generate circumferential contractile force which promotes tube elongation. In $Fbn2^{T2547A/T2547A}$ tracheas, aberrantly oriented SM cells restrict tube elongation by compressing the mesenchyme and attached epithelium, as in the case of SM restriction of gut elongation [4]. Chondrocytes have also been reported to be essential for tracheal tube expansion [36, 71]. Notably, *Sox9* knockout mice exhibit defects in chondrocyte differentiation, tracheal cartilage formation and tracheal tube expansion [36, 71]. It is thus possible that in $Fbn2^{T2547A/T2547A}$ tracheas the chondrocyte differentiation defects lead to impaired cartilage formation, ultimately resulting in the narrowed tracheal tube. Interestingly, animal models of tracheal stenosis including $Cftr^{-/-}$ and $Cav3.2^{-/-}$ mice both show cartilage ring and lumen formation defects [72-74], phenotypes similar to those observed in $Fbn2^{T2547A/T2547A}$ mice. *Cav3.2* regulates tracheal cartilage formation by promoting chondrocyte differentiation [74]. It is thus possible that a defect in chondrocyte differentiation is a common cause of congenital tracheal stenosis.

Here we reveal novel functions for FBN2 in elastic fiber formation and Fibronectin accumulation. *Fbn2* mutants exhibit no significant differences in elastic fiber formation in esophageal or vascular SM cells [45]. However, $Fbn1^{-/-}$ mice exhibit elastic fiber organization defects in aortic tissues [45]. $Fbn2^{T2547A/T2547A}$ esophagi exhibit WT-like p38 phosphorylation and *Mmp2* mRNA expression levels. *Fbn1* mutants exhibit increased p38 phosphorylation [75] as well as increased MMP2 and MMP9 levels in their thoracic aortas [76]. Interestingly, both $Fbn1^{-/+}$; $Fbn2^{-/-}$ and $Fbn1^{-/-}$; $Fbn2^{-/-}$ animals display a more severe vascular phenotype than $Fbn1^{-/-}$ mice [45], indicating that *Fbn1* and *Fbn2* perform partially overlapping functions during aortic development. It is thus possible that the absence of ECM defects in $Fbn2^{T2547A/T2547A}$ esophagi is due to functional redundancy with *Fbn1*. FBN1 promotes Tropoelastin coacervation [49], and prevents Elastin disruption and degradation possibly by decreasing MMP2 and MMP9 activity [50, 51]. However, $Fbn2^{T2547A/T2547A}$ tracheas appear to exhibit no obvious reduction in Elastin protein levels, indicating that FBN2

is required for elastic fiber formation but not protein expression during tracheal tube formation. Fibrillin microfibrils have been reported to colocalize and interact with Fibronectin [53, 54], and their deposition depends on Fibronectin assembly [77]. Interestingly, our studies suggest that Fibrillin microfibrils are also required for Fibronectin accumulation.

Our study presents a novel signaling axis governing ECM homeostasis, through Fibrillin microfibrils, p38 MAPK activation, and matrix metalloproteinases. *Fbn2* deficiency leads to aberrant activation of p38 MAPK signaling, which in turn induces an upregulation of MMP activity to disrupt elastic fiber formation and degrade Fibronectin. However, the exact mechanisms by which FBN2 regulates p38 activity and p38 modulates *Mmp* expression remain to be determined. TGF-β is abnormally activated in *Fbn2*-null osteoblasts [78]. Interestingly, TGF-β inhibition has been reported to decrease p38 phosphorylation in SM cells [79]. It is possible that absence of FBN2 function activates TGF-β signaling, thereby increasing p38 phosphorylation. Several targets of p38 MAPK have been reported to regulate *Mmp2* and *Mmp9* expression at the transcriptional level [67], and thus an increase in p38 phosphorylation might lead to the activation of specific transcription factor(s) whose target genes include *Mmp2* and *Mmp9*.

Fibrillin microfibrils have been found within the matrix of human cartilage [80], and *FBN2* mutations cause crumpled ears in patients [81, 82], which may be due to auricular cartilage defects. Our work presents evidence that Fibrillin microfibrils are required for cartilage formation possibly by promoting chondrocyte differentiation. Notably, FBN2 levels appear to be significantly decreased in the tracheal cartilage of tracheomalacia patients, suggesting that Fibrillin microfibrils are essential for cartilage formation also in humans. It will be interesting to investigate the underlying molecular mechanisms.

Mutations in *FBN2* have been associated with congenital contractural arachnodactyly [81-84] and vascular disease in humans [85] as well as endocardial morphogenesis defects in zebrafish [86]. Our *Fbn2* point mutant in mouse exhibits tracheal stenosis possibly caused by cartilage differentiation defects, providing a new model to study the etiology of this disease, and develop therapeutic approaches.

Acknowledgements

We thank Francesco Ramirez for providing *Fbn2* null mice, Radhan Ramadass and Yu Hsuan Carol Yang for imaging assistance, Rubén Marín-Juez, Paolo Panza, Konstantinos Gkatzis, Srinath Ramkumar, Khrievono Kikhi, Jason Kuan Han Lai, Sharon Meaney-Gardian and Nana Fukuda for discussion or assistance. Funding for this study was provided by the Deutsche Forschungsgemeinschaft (DFG) to G.S. (SFB829/ B11, B12) and the Max Planck Society to S.O and D.Y.R.S.

Author contributions

W.Y. and D.Y.R.S. conceived the project, designed experiments and analyzed data; W.Y., H.-T.K., F.G., R.L., B.G., C.B., D.S. and S.O. contributed to experiments and data analysis; S.W. performed western blot and trachea physiology experiments and data analysis; G.S. contributed to FBN2 antibody generation; W.Y. and D.Y.R.S. wrote the manuscript. All authors commented on the manuscript.

Conflict of interest

The authors declare that they have no conflict of interest.

References

1 Hogan BL, Kolodziej PA. Organogenesis: molecular mechanisms of tubulogenesis. *Nat Rev Genet* 2002; 3: 513-23

2 Iruela-Arispe M L, Beitel GJ. Tubulogenesis. *Development* 2013; 140: 2851-5.

3 Knot HJ, Nelson MT. Regulation of arterial diameter and wall [Ca2+] in cerebral arteries of rat by membrane potential and intravascular pressure. *J Physiol* 1998; 508: 199-209.

4 Shyer AE, Tallinen T, Nerurkar NL, *et al.* Villification: how the gut gets its villi. *Science* 2013; 342: 212-8.

5 Kim HY, Pang MF, Varner VD, *et al.* Localized Smooth Muscle Differentiation Is Essential for Epithelial Bifurcation during Branching Morphogenesis of the Mammalian Lung. *Dev Cell* 2015; 34: 719-26.

6 Hines EA, Jones MK, Verheyden JM, *et al.* Establishment of smooth muscle and cartilage juxtaposition in the developing mouse upper airways. *Proc Natl Acad Sci USA* 2013; 110: 19444-9.

7 Domyan ET, Sun X. Patterning and plasticity in development of the respiratory lineage. *Dev Dyn* 2011; 240: 477-85.

8 Elluru RG, Whitsett JA. Potential role of Sox9 in patterning tracheal cartilage ring formation in an embryonic mouse model. *Arch Otolaryngol Head Neck Surg* 2004; 130: 732-6.

9 Snowball J, Ambalavanan M, Whitsett J, *et al.* Endodermal Wnt signaling is required for tracheal cartilage formation. *Dev Biol* 2015; 405: 56-70.

10 Yin W, Kim HT, Wang S, *et al*. The potassium channel KCNJ13 is essential for smooth muscle cytoskeletal organization during mouse tracheal tubulogenesis. *Nat Commun* 2018; 9: 2815.

11 Miller LA, Wert SE, Clark JC, *et al.* Role of Sonic hedgehog in patterning of tracheal-bronchial cartilage and the peripheral lung. *Dev Dyn* 2004; 231: 57-71.

12 Rawlins EL, Ostrowski LE, Randell SH, *et al.* Lung development and repair: contribution of the ciliated lineage. *Proc. Natl. Acad. Sci. U S A* 2007; 104: 410–417.

13 Rawlins, EL, Clark CP, Xue Y, *et al.* The Id2+ distal tip lung epithelium contains individual multipotent embryonic progenitor cells. *Development* 2009; 136: 3741–3745.

14 Rock J R, Hogan BL. Epithelial Progenitor Cells in Lung Development, Maintenance, Repair, and Disease. *Annu Rev Cell Dev Biol* 2011; 27: 493-512.

15 Rackley CR, Stripp BR. Building and maintaining the epithelium of the lung. *J Clin Invest* 2012; 122: 2724–2730.
16 Landing BH, Dixon LG. Congenital malformations and genetic disorders of the respiratory tract (larynx, trachea, bronchi, and lungs. *Am Rev Respir Dis* 1979; 120: 151-85.
17. Fraga JC, Jennings RW, Kim PC. Pediatric tracheomalacia. *Semin Pediatr Surg* 2016; 25: 156-64.
18 Lubarsky B, Krasnow MA. Tube morphogenesis: making and shaping biological tubes. *Cell* 2003; 112: 19-28.
19 Andrew DJ, Ewald AJ. Morphogenesis of epithelial tubes: Insights into tube formation, elongation, and elaboration. *Dev Biol* 2010; 341: 34-55.
20 Sala FG, Del Moral PM, Tiozzo C, *et al.* FGF10 controls the patterning of the tracheal cartilage rings via Shh. *Development* 2011; 138: 273-82.
21 Gerhardt B, Leesman L, Burra K, *et al.* Notum attenuates Wnt/β-catenin signaling to promote tracheal cartilage patterning. *Dev Biol* 2018; 436: 14-27.
22 Yu W, Datta A, Leroy P, *et al.* Beta1-integrin orients epithelial polarity via Rac1 and laminin. *Mol Biol Cell* 2005; 16: 433-45.
23 Bryant DM, Roignot J, Datta A, *et al.* A molecular switch for the orientation of epithelial cell polarization. *Dev Cell* 2014; 31: 171-87.
24 Wang S, Sekiguchi R, Daley WP, *et al.* Patterned cell and matrix dynamics in branching morphogenesis. *J Cell Biol* 2017; 216: 559-570.
25 Li Q, Zhang Y, Pluchon P, *et al.* Extracellular matrix scaffolding guides lumen elongation by inducing anisotropic intercellular mechanical tension. *Nat Cell Biol* 2016; 18: 311-8.
26 Kile BT, Hentges KE, Clark AT, *et al*. Functional genetic analysis of mouse chromosome 11. *Nature* 2003; 425: 81-6.
27 Arteaga-Solis E, Gayraud B, Lee SY, *et al.* Regulation of limb patterning by extracellular microfibrils. *J Cell Biol* 2001; 154: 275-81.
28 Charbonneau NL, Carlson EJ, Tufa S, *et al*. In vivo studies of mutant fibrillin-1 microfibrils. *J Biol Chem* 2010; 285: 24943-55.
29 Rigueur D, Lyons KM. Whole-mount skeletal staining. *Methods Mol Biol* 2014; 1130: 113-121.
30 Gosset M, Berenbaum F, Thirion S, Jacques C. Primary culture and phenotyping of murine chondrocytes. *Nat Protoc* 2008; 3: 1253-60.
31 Komatsu, Y., Kishigami, S. & Mishina, Y. In situ hybridization methods for mouse whole mounts and tissue sections with and without additional β-galactosidase staining. *Methods Mol Biol* 2014; 1092: 1-15.
32 Pilecki B, Holm AT, Schlosser A, *et al* Characterization of Microfibrillar-associated Protein 4 (MFAP4) as a Tropoelastin- and Fibrillin-binding Protein Involved in Elastic Fiber Formation. *J Biol Chem* 2016; 291: 1103-14.
33 Del Moral PM, Warburton D. Explant culture of mouse embryonic whole lung, isolated epithelium, or mesenchyme under chemically defined conditions as a system to evaluate the molecular mechanism of branching morphogenesis and cellular differentiation. *Methods Mol Biol* 2010; 633: 71-9.

34 Bi W, Deng JM, Zhang Z, *et al.* Sox9 is required for cartilage formation. *Nat Genet* 1999; 22: 85-9.
35 Yanagino T, Yuasa K, Nagahama M, *et al.* Transcriptional regulation of fibrillin-2 gene by E2F family members in chondrocyte differentiation. *J Cell Biochem* 2009; 106: 580-8.
36 Kishimoto K, Tamura M, Nishita M, *et al*. Synchronized mesenchymal cell polarization and differentiation shape the formation of the murine trachea and esophagus. *Nat Commun* 2018; 9: 2816.
37 Li Y, Dudley AT. Noncanonical frizzled signaling regulates cell polarity of growth plate chondrocytes. *Development* 2009; 136: 1083-92.
38 Nobes CD, Hall A. Rho GTPases control polarity, protrusion, and adhesion during cell movement. *J Cell Biol* 1999; 22: 1235-44.
39 Kwon HB, Wang S, Helker CS, *et al*. In vivo modulation of endothelial polarization by Apelin receptor signalling. *Nat Commun*. 2016; 7:11805.
40 Knot HJ, Nelson MT. Regulation of arterial diameter and wall [Ca2+] in cerebral arteries of rat by membrane potential and intravascular pressure. *J Physiol* 1998; 508: 199-209.
41 Hannezo E, Dong B, Recho P, *et al.* Cortical instability drives periodic supracellular actin pattern formation in epithelial tubes. *Proc Natl Acad Sci U S A* 2015; 112: 8620-5.
42 Billmyre KK, Hutson M, Klingensmith J. One shall become two: Separation of the esophagus and trachea from the common foregut tube. *Dev Dyn* 2015; 244: 277-88.
43 Kablar B, Tajbakhsh S, Rudnicki MA. Transdifferentiation of esophageal smooth to skeletal muscle is myogenic bHLH factor-dependent. *Development* 2000; 127: 1627-39.
44 Bunton TE, Biery NJ, Myers L, *et al.* Phenotypic alteration of vascular smooth muscle cells precedes elastolysis in a mouse model of Marfan syndrome. *Circ Res* 2001; 88: 37-43.
45 Carta L, Pereira L, Arteaga-Solis E, *et al*. Fibrillins 1 and 2 perform partially overlapping functions during aortic development. *J Biol Chem* 2006; 281: 8016-23.
46 Kielty CM. Elastic fibres in health and disease. *Expert Rev Mol Med* 2006 8: 1-23.
47 Lucero HA, Kagan HM. Lysyl oxidase: an oxidative enzyme and effector of cell function. *Cell Mol Life Sci* 2006; 63: 2304-16.
48 Jensen SA, Robertson IB, Handford PA. Dissecting the fibrillin microfibril: structural insights into organization and function. *Structure* 2012; 20: 215-25.
49 Clarke AW, Wise SG, Cain SA, *et al*. Coacervation is promoted by molecular interactions between the PF2 segment of fibrillin-1 and the domain 4 region of tropoelastin. *Biochemistry* 2005; 44: 10271-81.
50 Schwill S, Seppelt P, Grünhagen J, *et al*. The fibrillin-1 hypomorphic mgR/mgR murine model of Marfan syndrome shows severe elastolysis in all segments of the aorta. *J Vasc Surg* 2013; 57: 1628-36.
51 Ju X, Ijaz T, Sun H, *et al*. IL-6 regulates extracellular matrix remodeling associated with aortic dilation in a fibrillin-1 hypomorphic mgR/mgR mouse model of severe Marfan syndrome. *J Am Heart Assoc* 2014; 3: e000476.
52 Hubmacher D, Wang LW, Mecham RP, *et al.* Adamtsl2 deletion results in bronchial fibrillin microfibril accumulation and bronchial epithelial dysplasia--a novel mouse model providing insights into geleophysic dysplasia. *Dis Model Mech* 2015; 8: 487-99.

53 Pierschbacher MD, Ruoslahti E. Cell attachment activity of fibronectin can be duplicated by small synthetic fragments of the molecule. *Nature* 1984; 309: 30-3.
54 Sabatier L, Chen D, Fagotto-Kaufmann C, *et al*. Fibrillin assembly requires fibronectin. *Mol Biol Cell* 2009; 20: 846-58.
55 Martins GG, Rifes P, Amândio R, *et al*. Dynamic 3D cell rearrangements guided by a fibronectin matrix underlie somitogenesis. *PLoS One* 2009; 4: e7429.
56 Vaz R, Martins GG, Thorsteinsdóttir S, *et al*. Fibronectin promotes migration, alignment and fusion in an in vitro myoblast cell model. *Cell Tissue Res* 2012; 348: 569-78.
57 Ray D, Osmundson EC, Kiyokawa H. Constitutive and UV-induced fibronectin degradation is a ubiquitination-dependent process controlled by beta-TrCP. *J Biol Chem* 2006; 281: 23060-5.
58 Li DY, Brooke B, Davis EC, *et al*. Elastin is an essential determinant of arterial morphogenesis. *Nature* 1998; 393: 276-80.
59 Wagenseil JE, Ciliberto CH, Knutsen RH, *et al*. Reduced vessel elasticity alters cardiovascular structure and function in newborn mice. *Circ Res* 2009; 104: 1217-24.
60 Kenny HA , Kaur S, Coussens LM, *et al*. The initial steps of ovarian cancer cell metastasis are mediated by MMP-2 cleavage of vitronectin and fibronectin. *J Clin Invest* 2008; 118: 1367-79.
61 Yabluchanskiy A, Ma Y, Iyer RP, *et al*. Matrix metalloproteinase-9: Many shades of function in cardiovascular disease. *Physiology* 2013; 28: 391-403.
62 Oller J, Méndez-Barbero N, Ruiz EJ, *et al*. Nitric oxide mediates aortic disease in mice deficient in the metalloprotease Adamts1 and in a mouse model of Marfan syndrome. *Nat Med* 2017; 23: 200-212.
63 Kim HT, Yin W, Jin YJ, *et al*. *Myh10* deficiency leads to defective extracellular matrix remodeling and pulmonary disease. *Nat Commun.* in press (2018).
64 Grobelny D, Poncz L, Galardy RE, *et al*. Inhibition of human skin fibroblast collagenase, thermolysin, and Pseudomonas aeruginosa elastase by peptide hydroxamic acids. *Biochemistry* 1992; 31: 7152-4.
65 Skjøt-Arkil H, Clausen RE, Nguyen QH, *et al*. Measurement of MMP-9 and -12 degraded elastin (ELM) provides unique information on lung tissue degradation. *BMC Pulm Med* 2012; 12: 34.
66 Gill SE, Pape MC, Leco KJ, *et al*. Tissue inhibitor of metalloproteinases 3 regulates extracellular matrix--cell signaling during bronchiole branching morphogenesis. *Dev Biol* 2006; 298: 540-54.
67 Koul HK, Pal M, Koul S. Role of p38 MAP Kinase Signal Transduction in Solid Tumors. *Genes Cancer* 2013; 4: 342-59.
68 Song H, Ki SH, Kim SG, *et al*. Activating transcription factor 2 mediates matrix metalloproteinase-2 transcriptional activation induced by p38 in breast epithelial cells. *Cancer Res* 2006; 66: 10487-96.
69 Kumar B, Koul S, Petersen J, *et al*. p38 mitogen-activated protein kinase-driven MAPKAPK2 regulates invasion of bladder cancer by modulation of MMP-2 and MMP-9 activity. *Cancer Res* 2010; 70: 832-41.

70 Cuenda A, Rouse J, Doza YN, *et al*. SB 203580 is a specific inhibitor of a MAP kinase homologue which is stimulated by cellular stresses and interleukin-1. *FEBS Lett* 1995; 364: 229-33.
71 Turcatel G, Rubin N, Menke DB, *et al.* Lung mesenchymal expression of Sox9 plays a critical role in tracheal development. *BMC Biol* 2013; 11: 117.
72 Bonvin E, Le Rouzic P, Bernaudin JF, *et al*. Congenital tracheal malformation in cystic fibrosis transmembrane conductance regulator-deficient mice. *J Physiol* 2008; 586: 3231-43.
73 Wallace HL, Southern KW, Connell MG, *et al*. Abnormal tracheal smooth muscle function in the CF mouse. *Physiol Rep*. 2013; 1: e00138.
74 Lin SS, Tzeng BH, Lee KR, *et al*. Cav3.2 T-type calcium channel is required for the NFAT-dependent Sox9 expression in tracheal cartilage. *Proc Natl Acad Sci U S A* 2014; 111: E1990-8.
75 Carta L, Smaldone S, Zilberberg L, *et al*. p38 MAPK is an early determinant of promiscuous Smad2/3 signaling in the aortas of fibrillin-1 (Fbn1)-null mice. *J Biol Chem* 2009; 284: 5630-6.
76 Xiong W, Knispel RA, Dietz HC, *et al*. Doxycycline delays aneurysm rupture in a mouse model of Marfan syndrome. *J Vasc Surg* 2008; 47: 166-72.
77 Kinsey R, Williamson MR, Chaudhry S, *et al*. Fibrillin-1 microfibril deposition is dependent on fibronectin assembly. *J Cell Sci* 2008; 121: 2696-704.
78 Nistala H, Lee-Arteaga S, Smaldone S, *et al.* Fibrillin-1 and -2 differentially modulate endogenous TGF-β and BMP bioavailability during bone formation. *J Cell Biol.* 2010; 190: 1107-21.
79 Granata A, Serrano F, Bernard WG, et al. An iPSC-derived vascular model of Marfan syndrome identifies key mediators of smooth muscle cell death. *Nat Genet.* 2017; 49: 97-109.
80 Keene DR, Jordan CD, Reinhardt DP, *et al*. Fibrillin-1 in human cartilage: developmental expression and formation of special banded fibers. *J Histochem Cytochem* 1997; 45: 1069-82.
81 Mehar V, Yadav D, Kumar R, *et al*. Congenital contractural arachnodactyly due to a novel splice site mutation in the FBN2 gene. *J Pediatr Genet* 2014; 3: 163-6.
82 Lavillaureix A, Heide S, Chantot-Bastaraud S, *et al*. Mosaic intragenic deletion of FBN2 and severe congenital contractural arachnodactyly. *Clin Genet* 2017; 92: 556-558.
83 Putnam EA, Zhang H, Ramirez F, *et al*. Fibrillin-2 (FBN2) mutations result in the Marfan-like disorder, congenital contractural arachnodactyly. *Nat Genet* 1995; 11: 456-8.
84 Gupta PA, Wallis DD, Chin TO, *et al*. FBN2 mutation associated with manifestations of Marfan syndrome and congenital contractural arachnodactyly. *J Med Genet* 2004; 41: e56.
85 Kunnas T, Solakivi T, Nikkari ST, *et al*. Gene polymorphisms of fibronectin rs2289202 and fibrillin 2 rs331069 associate with vascular disease, the TAMRISK study. *Biomed Rep* 2018; 8: 65-68.
86 Mellman K, Huisken J, Dinsmore C, *et al*. Fibrillin-2b regulates endocardial morphogenesis in zebrafish. *Dev Biol* 2012; 372: 111-9.

Figure Legends

FIGURE 1 *Fbn2*$^{T2547A/T2547A}$ mice exhibit tracheal tube formation defects. a) Representative gross morphology of P0 WT (n=16) and mutants (n=16). b) Quantification of body weight of P0 WT (n=15) and mutants (n=15). c) Representative images of ventral views of wholemount tracheas stained with alcian blue from P0 WT (n=24) and mutants (n=24). Double-sided arrows indicate tracheal tube length. Arrows point to tracheal cartilage rings. d) Quantification of P0 WT (n=15) and mutant (n=15) tracheal tube length. e) Quantification of the number of tracheal cartilage rings from P0 WT (n=15) and mutants (n=15). f) Representative images of transverse sections of tracheas stained with hematoxylin and eosin from P0 WT (n=5) and mutants (n=5). g) Quantification of tracheal lumen area from P0 WT (n=5) and mutants (n=5). h) Whole-exome sequencing of WT control (*Fbn2* heterozygous, n=2) and mutant (*Fbn2* homozygous, n=2) samples. Green indicates the WT nucleotide A. Red indicates the mutant nucleotide T. i) Sequence of WT and mutant genomic DNA around the lesion. DNA sequence chromatograms show TGT for cysteine in WT (n=112) (left), TGT and TGA in heterozygous mutants, and TGA for the stop codon in homozygous mutants (n=124) (right). Arrows point to the mutation site. j) Evolutionary conservation of the p.C849 residue in vertebrates. k) Domain structure of WT FBN2 and FBN2^{C849X}. l) Representative images of ventral views of wholemount tracheas stained with alcian blue from P0 WT (n=15) and *Fbn2*$^{-/T2547A}$ double heterozygous animals (n=15). Double-sided arrows indicate tracheal tube length. Arrows point to tracheal cartilage rings. Scale bars: 1 mm (c, l), 200 μm (f). ***P* < 0.05; ****P* < 0.01; *****P* < 0.001; Unpaired Student‟s *t*-test, mean ± s.d. WT, Wild-Type; MT, Mutant; A, Anterior; P, Posterior; D, Dorsal; V, Ventral; L, Left; R, Right; Cart, Cartilage; SM, Smooth muscle.

FIGURE 2 FBN2 localizes around the tracheal SM cells and chondroblasts. a) Immunostaining for FBN2 (green) and αSMA (red), and DAPI staining (blue) of transverse sections of WT tracheas (n=6) in the whole tracheal region (E12.5) or mostly in SM regions at later stages. b) Immunostaining for FBN2 (green) and SOX9 (red), and DAPI staining (blue) of transverse sections of WT tracheas (n=6) mostly in cartilage regions at several embryonic and postnatal stages. c) RT–qPCR analysis of *Fbn2* expression in E12.5 WT (n=4) and *Fbn2* $^{T2547A/T2547A}$ (*n*=4) tracheas. d) Western blotting for FBN2 and GAPDH in P7 WT (n=4) and *Fbn2*$^{T2547A/T2547A}$ (n=4) tracheas. e) Immunostaining for FBN2 (green) and αSMA (red), and DAPI staining (blue) of transverse sections of E14.5 *Fbn2* $^{T2547A/T2547A}$ tracheas (n=6). Scale bars: 100 μm (e), 50 μm (a, b). ***P* < 0.05; Unpaired Student‟s *t*-test, mean ± s.d.

FIGURE 3 *Fbn2*$^{T2547A/T2547A}$ mice display defects in tracheal elongation, cartilage ring formation and SM organization. a) Representative images of ventral views of WT (n=6) and *Fbn2*$^{T2547A/T2547A}$ (n=6) tracheas at several embryonic stages. Double-sided arrows indicate tracheal tube length. b) Representative images of ventral views of WT (n=6) and *Fbn2*$^{T2547A/T2547A}$ (n=6) tracheas at postnatal stages. Double-sided arrows indicate tracheal tube length. c) Quantification of WT (n=6) and *Fbn2*$^{T2547A/T2547A}$ (n=6) tracheal tube length. d) Ventral views of SOX9 immunostaining (green) of WT (n=7) and *Fbn2*$^{T2547A/T2547A}$ (n=7) tracheas at several embryonic stages. Arrows point to tracheal rings. e) Representative

images of ventral views of wholemount tracheas stained with alcian blue from 15-months-old WT (n=7) and *Fbn2*$^{T2547A/T2547A}$ mice (n=7). Arrows point to tracheal cartilage rings. f) Quantification of the number of tracheal cartilage rings in WT (n=7) and *Fbn2*$^{T2547A/T2547A}$ (n=7) animals. g) Quantification of the distance between tracheal rings in WT (n=7) and *Fbn2*$^{T2547A/T2547A}$ (n=7) animals. h) Quantification of the ring width in WT (n=7) and *Fbn2*$^{T2547A/T2547A}$ (n=7) animals. i) Dorsal views of αSMA immunostaining (red) of WT (n=6) and *Fbn2*$^{T2547A/T2547A}$ (n=6) tracheas at several embryonic and postnatal stages. j) Quantification of SM area in WT (n=6) and *Fbn2*$^{T2547A/T2547A}$ (n=6) animals. Scale bars: 2 mm (b, e), 1 mm (a, d), 100 μm (i). ***P* < 0.05; ****P* < 0.01; NS, not significant; Unpaired Student‟s *t*-test, mean ± s.d.

FIGURE 4 *Fbn2* regulates SM cell orientation and polarization. a) Immunostaining for αSMA (red) and CDH1 (green), and DAPI staining (blue) of transverse sections of WT tracheas (n=6) at several embryonic stages. b) Quantification of tracheal SM cell nuclear aspect ratio (NAR). c) Dorsal views of αSMA immunostaining (red) and DAPI staining (blue) of WT (n=7) and *Fbn2*$^{T2547A/T2547A}$ (n=7) tracheas at several embryonic and postnatal stages. d) Quantification of WT (n=7) and *Fbn2*$^{T2547A/T2547A}$ (n=7) tracheal SM cell orientation. e) Dorsal views of αSMA (red) and GM130 (green) immunostaining and DAPI staining (blue) of E14.5 WT (n=6) and *Fbn2*$^{T2547A/T2547A}$ (n=6) tracheas. f) Quantification of E14.5 WT (n=6) and *Fbn2*$^{T2547A/T2547A}$ (n=6) Golgi apparatus position relative to the nucleus (blue). g) Dorsal views of time-lapse images of spontaneous contractions of E13.5 WT (n=6) and *Fbn2*$^{T2547A/T2547A}$ (n=6) tracheas. Lines indicate tracheal SM width. h) Quantification of contracting time of E13.5 WT (n=6) and *Fbn2*$^{T2547A/T2547A}$ (n=6) tracheas. i) Quantification of the amplitude of contractions of E13.5 WT (n=6) and *Fbn2*$^{T2547A/T2547A}$ (n=6) tracheas. j) Tracheal tension of P1 WT (n=5) and *Fbn2*$^{T2547A/T2547A}$ (n=5) tracheas. Scale bars: 50 μm (a, g), 20 μm (c, e). ***P* < 0.05; ****P* < 0.01; NS, not significant; Unpaired Student‟s *t*-test, mean ± s.d.

FIGURE 5 *Fbn2* modulates elastic fiber formation and Fibronectin accumulation. a) Dorsal views of αSMA (red) and Tropoelastin (green) immunostaining and DAPI staining (blue) of E14.5 WT (n=8) and *Fbn2*$^{T2547A/T2547A}$ (n=8) tracheas. Arrows point to short elastic fibers. b, c) Quantification of elastic fiber orientation (b) and short elastic fibers (c) around tracheal SM cells in WT (n=8) and *Fbn2*$^{T2547A/T2547A}$ (n=8) tracheas. d) Western blotting for Fibronectin, Elastin and GAPDH in P7 WT (n=7) and *Fbn2*$^{T2547A/T2547A}$ (n=7) tracheas. e) Quantification of relative levels of Fibronectin in P7 WT (n=7) and *Fbn2*$^{T2547A/T2547A}$ (n=7) tracheas. f) Dorsal views of αSMA (red) and Fibronectin (green) immunostaining and DAPI staining (blue) of E14.5 WT (n=8) and *Fbn2*$^{T2547A/T2547A}$ (n=8) tracheas. g) Quantification of mean fluorescence intensity of Fibronectin immunostaining in E14.5 WT (n=8) and *Fbn2*$^{T2547A/T2547A}$ (n=8) tracheas. h) RT–qPCR analysis of *Fibronectin* expression in E14.5 WT (n=5) and *Fbn2*$^{T2547A/T2547A}$ (*n*=5) tracheas. i) Western blotting for Fibronectin and GAPDH in P7 WT (n=5) and *Fbn2*$^{T2547A/T2547A}$ (n=5) ddH_2O-treated tracheas, and in *Fbn2*$^{T2547A/T2547A}$ methylamine hydrochloride-treated tracheas (n=5). j) Quantification of relative levels of Fibronectin in P7 WT (n=5) and *Fbn2*$^{T2547A/T2547A}$ (n=5) ddH_2O-treated tracheas, and in *Fbn2*$^{T2547A/T2547A}$ methylamine hydrochloride (MA)-treated tracheas (*n*=5). k)

Representative images of ventral views of E13.5 tracheas after treatment for 28 hours with DMEM/F-12 medium (n=6), 2 mU/ml elastase (n=6) or 2 mU/ml collagenase type II (n=6). l) Quantification of relative tracheal tube length after treatment for 28 hours with DMEM/F-12 medium (n=6), 2 mU/ml elastase (n=6) or 2 mU/ml collagenase type II (n=6). m) Dorsal views of αSMA immunostaining (red) and DAPI staining (blue) of E13.5 tracheas after treatment for 28 hours with DMEM/F-12 medium (n=6), 2 mU/ml elastase (n=6) or 2 mU/ml collagenase type II (n=6). n) Quantification of tracheal SM cell orientation after treatment for 28 hours with DMEM/F-12 medium (n=6) or 2 mU/ml elastase (n=6) or 2 mU/ml collagenase type II (n=6). Scale bars: 1 mm (k), 20 μm (a, f, m). $^{*}P < 0.05$; $^{**}P < 0.01$; NS, not significant; Unpaired Student‟s *t*-test, mean ± s.d.

FIGURE 6 MMPs function as mediators of FBN2 function in tracheal development. a) RT–qPCR analysis of *Mmp2* and *Mmp9* expression in E14.5 and P7 WT (n=5 and 5) and $Fbn2^{T2547A/T2547A}$ (n=5 and 5) tracheas. b) Western blotting for MMP2, MMP9 and GAPDH in P7 WT (n=7) and $Fbn2^{T2547A/T2547A}$ (n=7) tracheas. c) Quantification of relative levels of MMP2 and MMP9 in P7 WT (n=7) and $Fbn2^{T2547A/T2547A}$ (n=7) tracheas. d) Zymography analysis of MMP2 and MMP9 activity in P7 WT (n=6) and $Fbn2^{T2547A/T2547A}$ (n=6) tracheal extracts. e) Quantification of MMP2 and MMP9 activity in P7 WT (n=6) and $Fbn2^{T2547A/T2547A}$ (n=6) tracheal extracts. f) Representative images of ventral views of E15.5 WT (n=6) and $Fbn2^{T2547A/T2547A}$ (n=6) tracheas after DMSO injection, and $Fbn2^{T2547A/T2547A}$ tracheas (n=6) after GM6001 injection. Double-sided arrows indicate tracheal tube length. g) Quantification of E15.5 WT (n=6) and $Fbn2^{T2547A/T2547A}$ (n=6) tracheal tube length after DMSO injection, and $Fbn2^{T2547A/T2547A}$ tracheas (n=6) after GM6001 injection. h) Dorsal views of αSMA (red) and Tropoelastin (green), or Fibronectin (green) immunostaining and DAPI staining (blue) of E15.5 WT (n=6) and $Fbn2^{T2547A/T2547A}$ (n=6) tracheas after DMSO injection, and $Fbn2^{T2547A/T2547A}$ tracheas (n=6) after GM6001 injection. i-l) Quantification of tracheal SM cell orientation (i), elastic fiber orientation (j), short elastic fibers (k) and mean fluorescence intensity of Fibronectin immunostaining (l) in E15.5 WT (n=6) and $Fbn2^{T2547A/T2547A}$ (n=6) tracheas after DMSO injection, and in $Fbn2^{T2547A/T2547A}$ tracheas (n=6) after GM6001 injection. Scale bars: 1 mm (f), 20 μm (h). $^{*}P < 0.05$; $^{**}P < 0.01$; Unpaired Student‟s *t*-test, mean ± s.d.

FIGURE 7 Increased p38 signaling correlates with increased *Mmp* expression, impaired elastic fiber formation and Fibronectin degradation. a) Western blotting for phospho-p38, total p38 and GAPDH in P7 WT (n=7) and $Fbn2^{T2547A/T2547A}$ (n=7) tracheas. b) Quantification of relative levels of phospho-p38 in P7 WT (n=7) and $Fbn2^{T2547A/T2547A}$ (n=7) tracheas. c) RT–qPCR analysis of *Mmp2* and *Mmp9* expression in E14.5 WT (n=5) and $Fbn2^{T2547A/T2547A}$ (n=5) DMSO-treated tracheas, and in $Fbn2^{T2547A/T2547A}$ SB203580-treated tracheas (*n*=5). d) Representative images of ventral views of E15.5 WT (n=6) and $Fbn2^{T2547A/T2547A}$ (n=6) tracheas after DMSO injection, and $Fbn2^{T2547A/T2547A}$ tracheas (n=6) after SB203580 injection. Double-sided arrows indicate tracheal tube length. e) Quantification of tracheal tube length in E15.5 WT (n=6) and $Fbn2^{T2547A/T2547A}$ (n=6) after DMSO injection, and in $Fbn2^{T2547A/T2547A}$ (n=6) after SB203580 injection. f) Dorsal views of αSMA (red) and Tropoelastin (green), or Fibronectin (green) immunostaining and DAPI

staining (blue) of E15.5 WT (n=6) and *Fbn2*$^{T2547A/T2547A}$ (n=6) tracheas after DMSO injection, and *Fbn2*$^{T2547A/T2547A}$ tracheas (n=6) after SB203580 injection. g-j) Quantification of tracheal SM cell orientation (g), elastic fiber orientation (h), short elastic fibers, (i) and mean fluorescence intensity of Fibronectin immunostaining (j) in E15.5 WT (n=6) and *Fbn2*$^{T2547A/T2547A}$ (n=6) tracheas after DMSO injection, and in *Fbn2*$^{T2547A/T2547A}$ tracheas (n=6) after SB203580 injection. k) Proposed model for the effects of the *Fbn2*^{T2547A} mutation on ECM organization and stability, and tracheal SM cell orientation. Scale bars: 1 mm (d), 20 μm (f). *****$P < 0.05$; ******$P < 0.01$; Unpaired Student‟s *t*-test, mean ± s.d.

FIGURE 8 FBN2 and Fibronectin levels are decreased in the tracheas of human tracheomalacia patients. a) Representative images of transverse sections of tracheas stained with hematoxylin and eosin from healthy controls (n=5) and tracheomalacia patients (n=7). Arrows point to tracheal cartilage. b) Immunostaining for SOX9 (red) and FBN2 (green), and DAPI staining (blue) of transverse sections of ventral parts of tracheas from healthy controls (n=4) and tracheomalacia patients (n=6). c) Quantification of relative mean fluorescence intensity of FBN2 immunostaining in ventral parts of tracheas from healthy controls (n=4) and tracheomalacia patients (n=6). d) Immunostaining for SOX9 (red) and Fibronectin (green), and DAPI staining (blue) of transverse sections of ventral parts of tracheas from healthy controls (n=5) and tracheomalacia patients (n=5). e) Quantification of relative mean fluorescence intensity of Fibronectin immunostaining in ventral parts of tracheas from healthy controls (n=5) and tracheomalacia patients (n=5). Scale bars: 1 mm (a), 100 μm (b, d). *****$P < 0.05$; Unpaired Student‟s *t*-test, mean ± s.d.

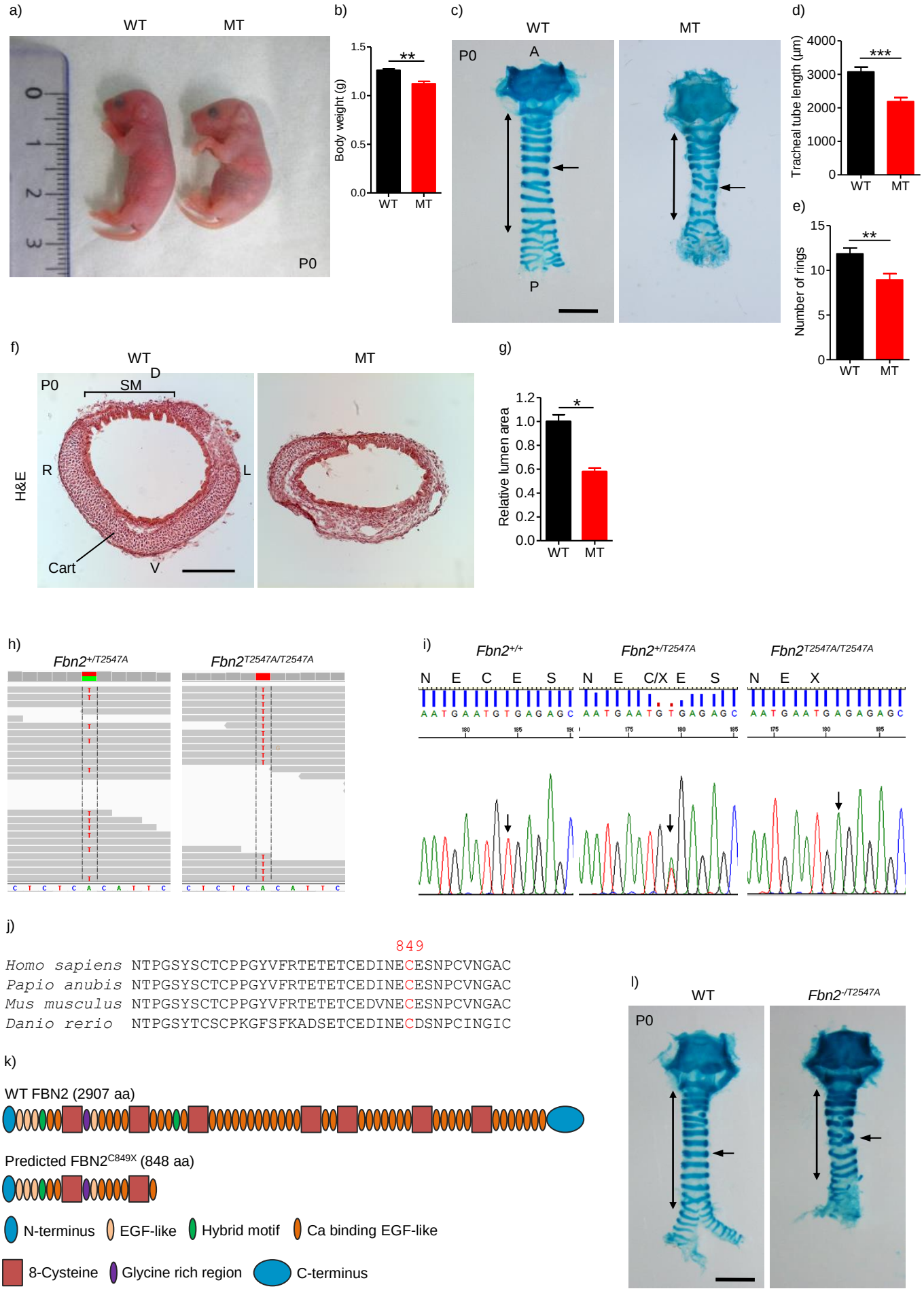

Yin et al., Fig. 1.

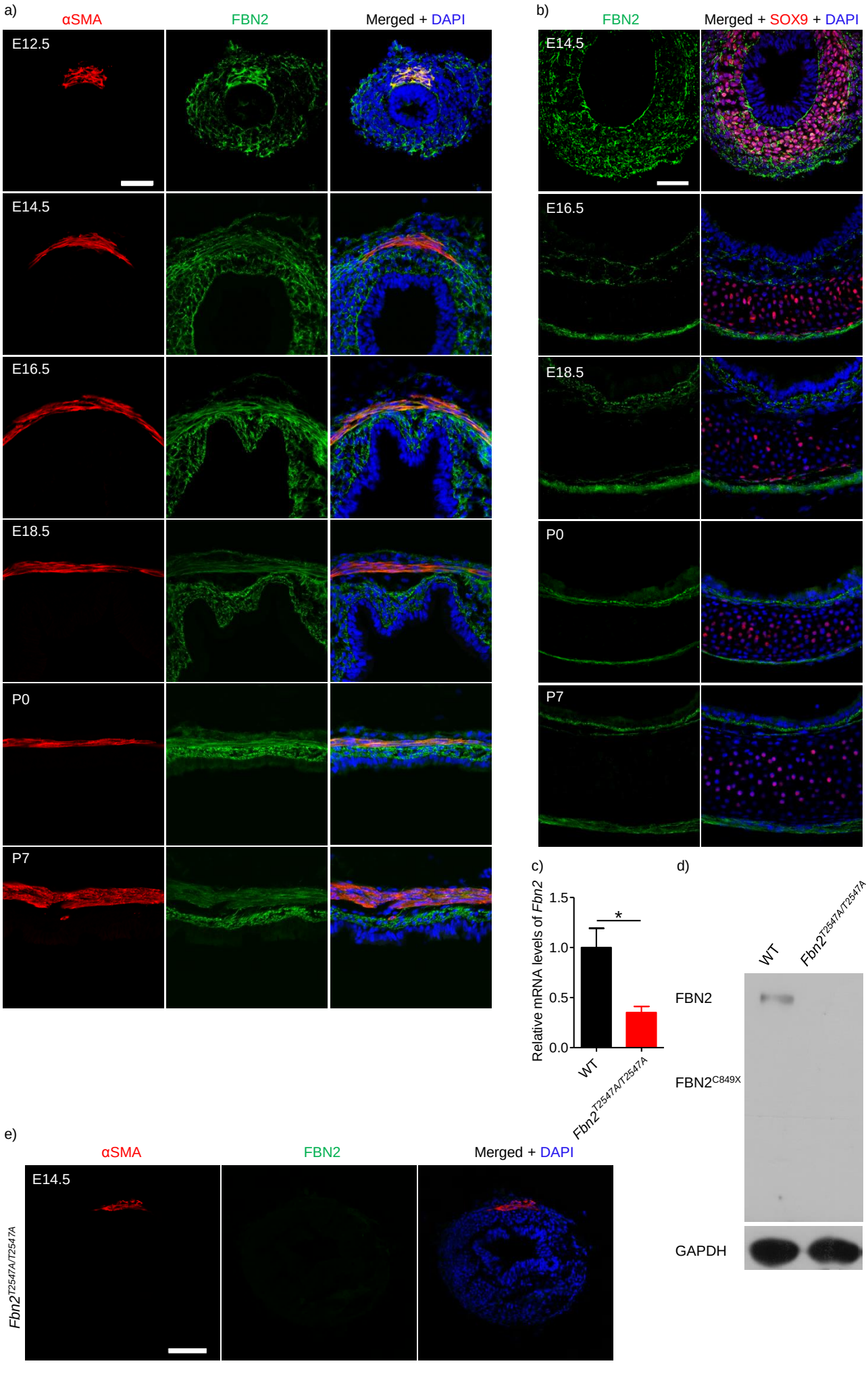

Yin et al., Fig. 2.

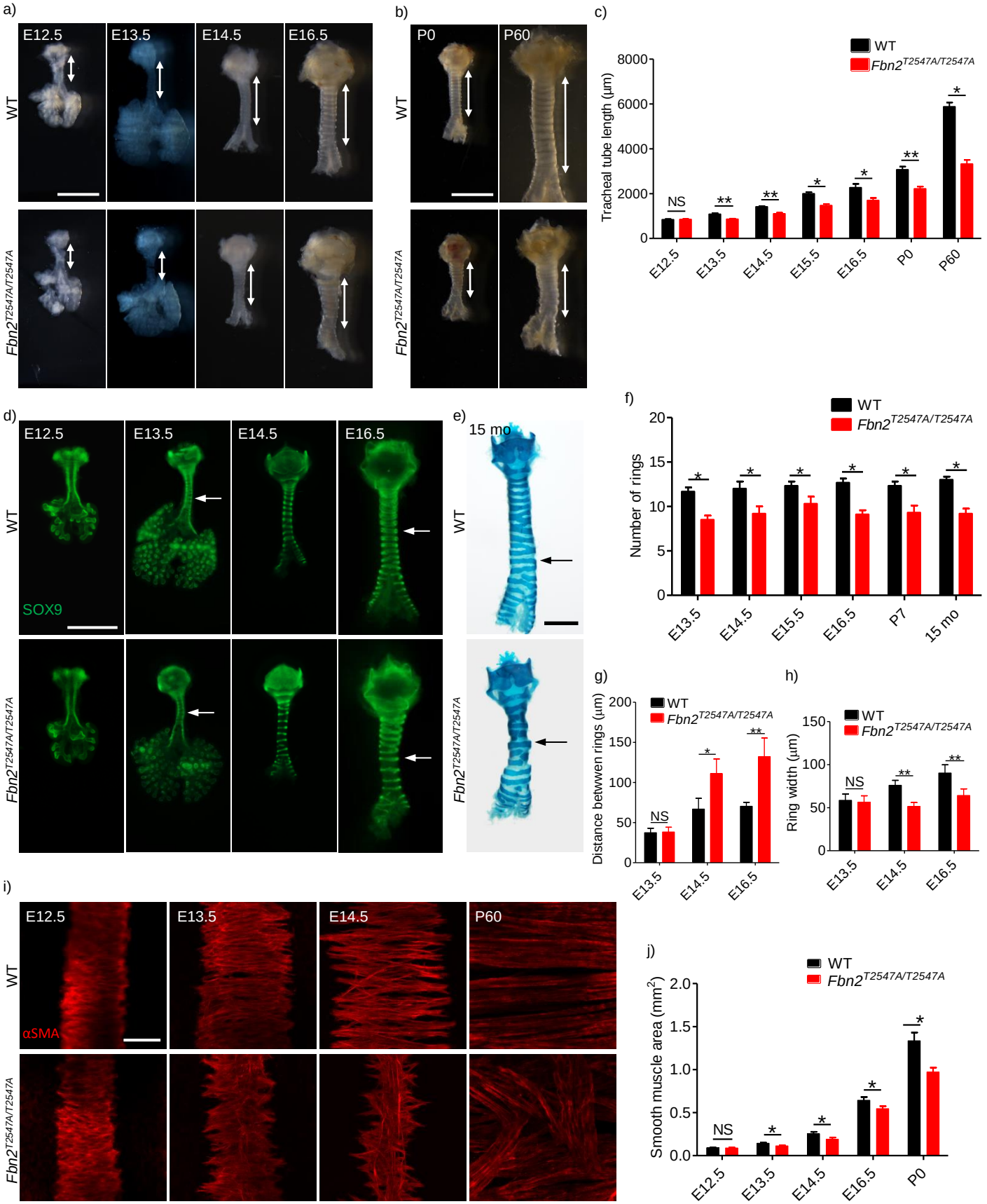

Yin et al., Fig. 3.

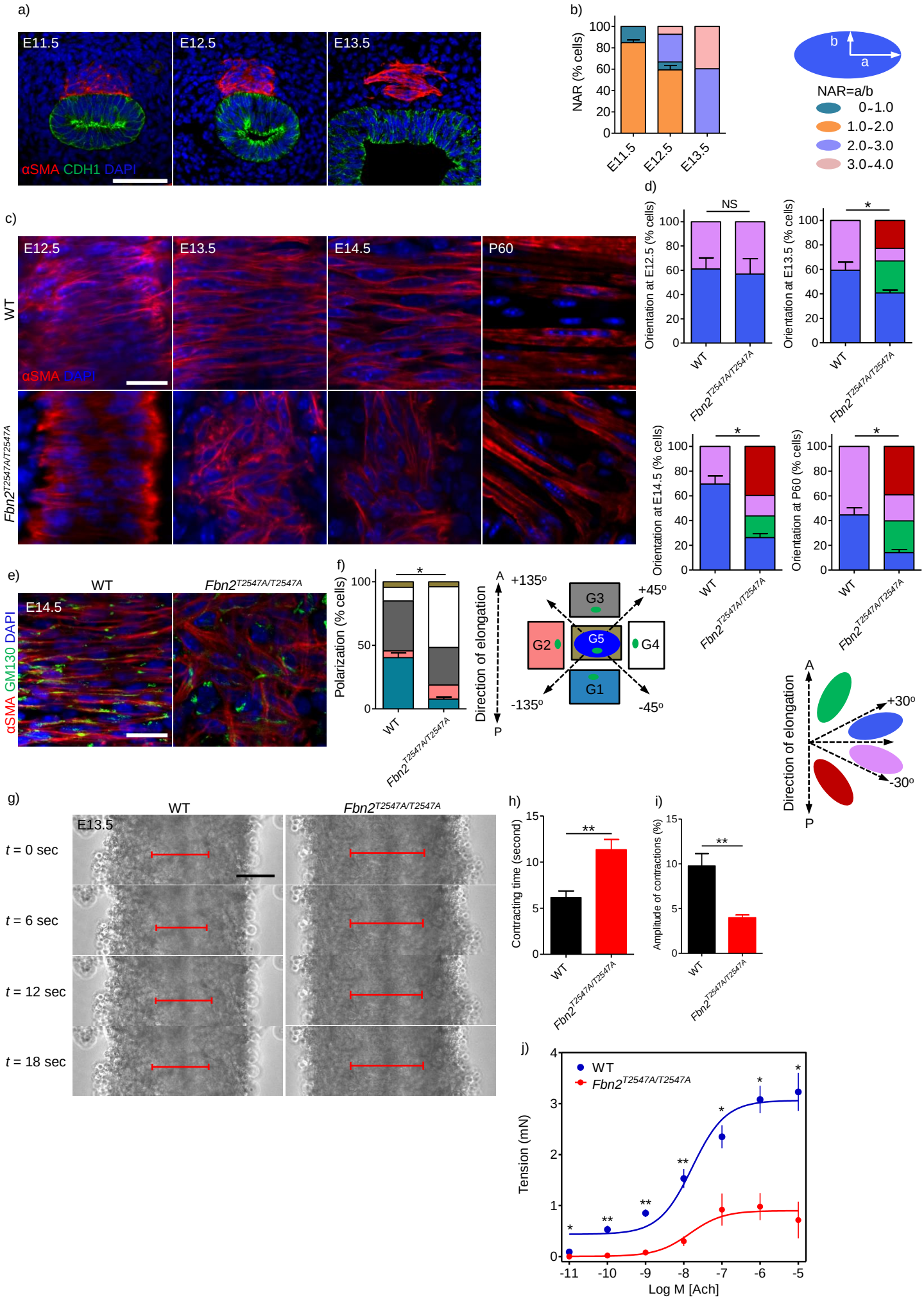

Yin et al., Fig. 4.

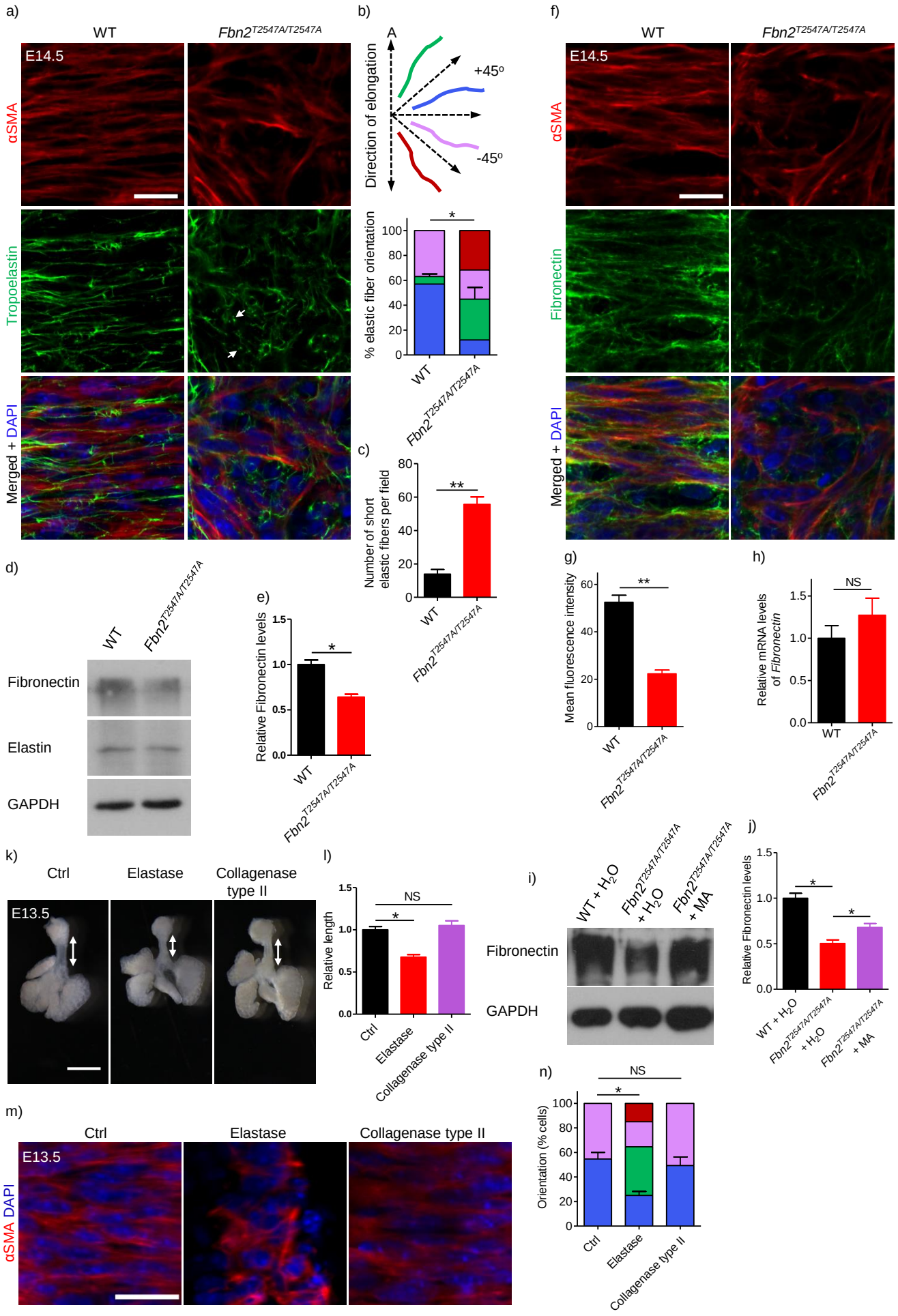

Yin et al., Fig. 5.

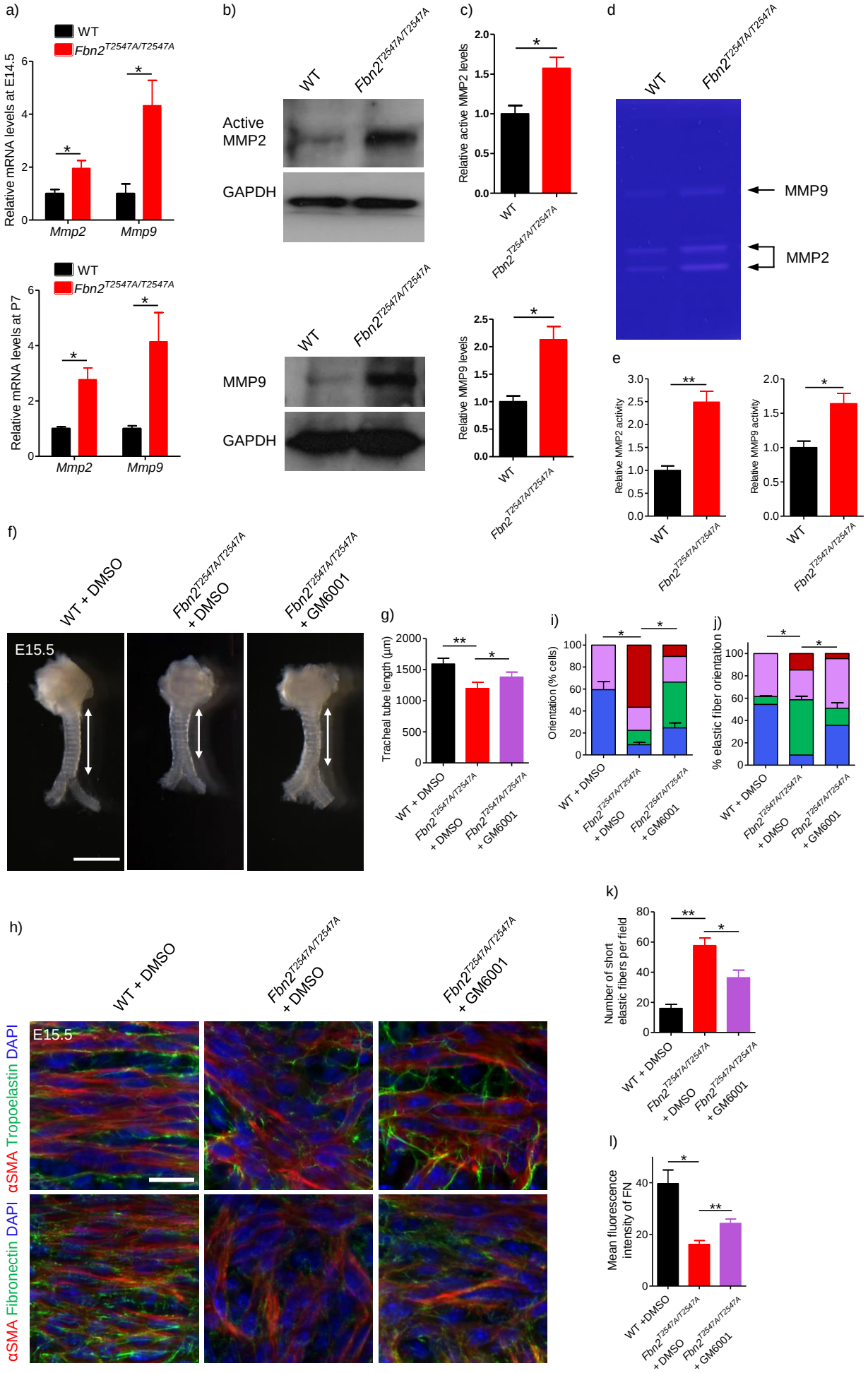

Yin et al., Fig. 6.

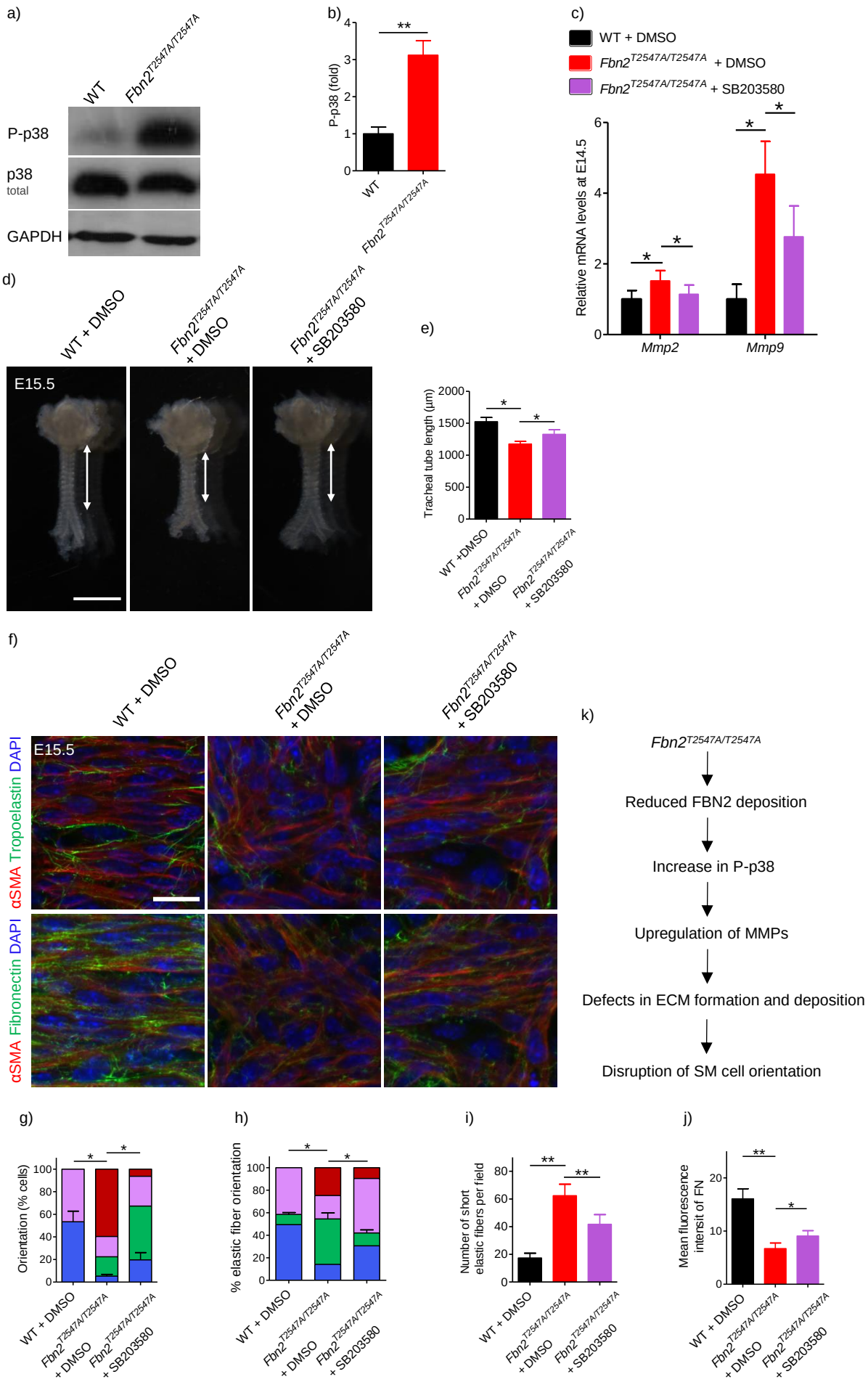

Yin et al., Fig. 7.

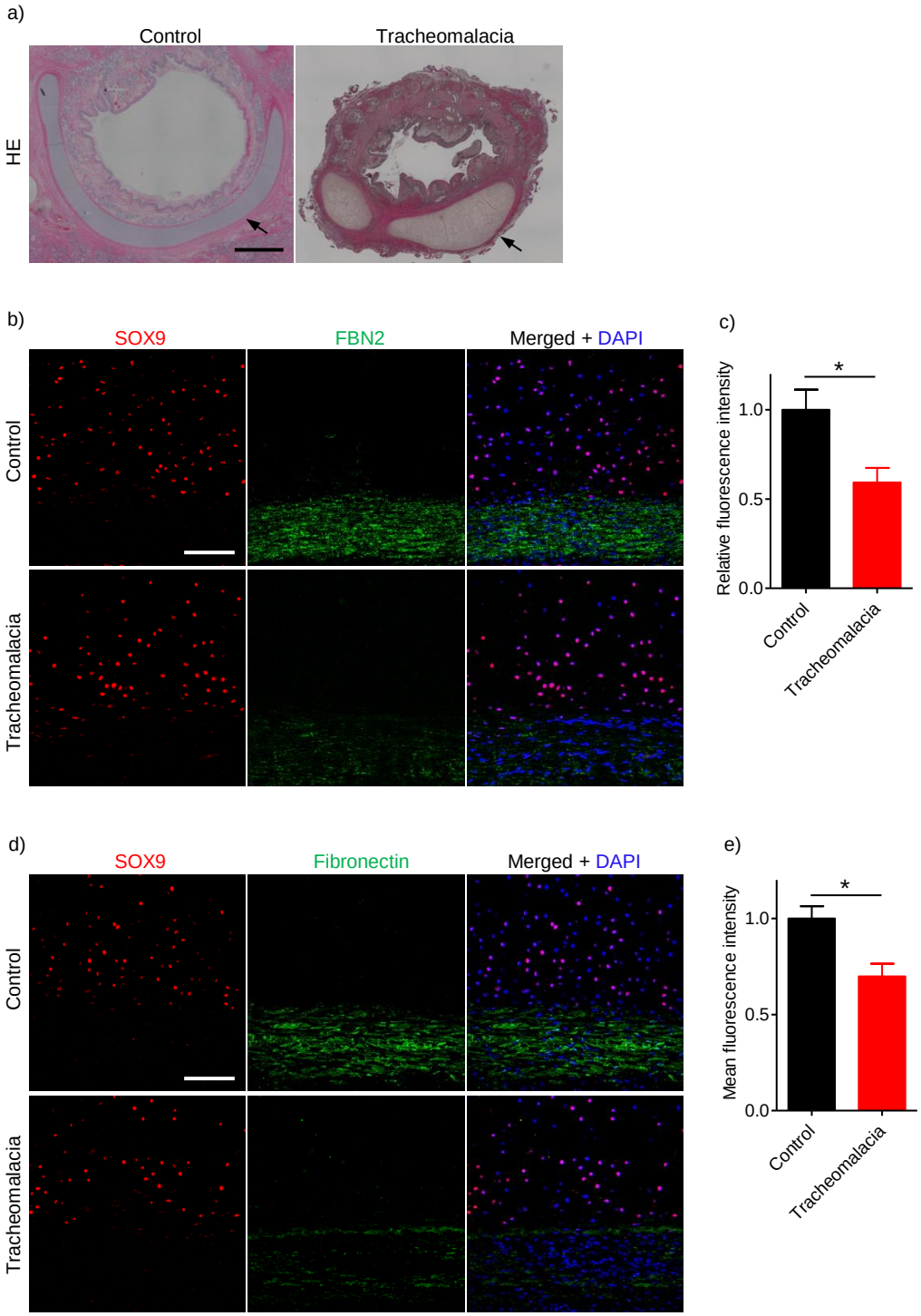

Yin et al., Fig. 8.

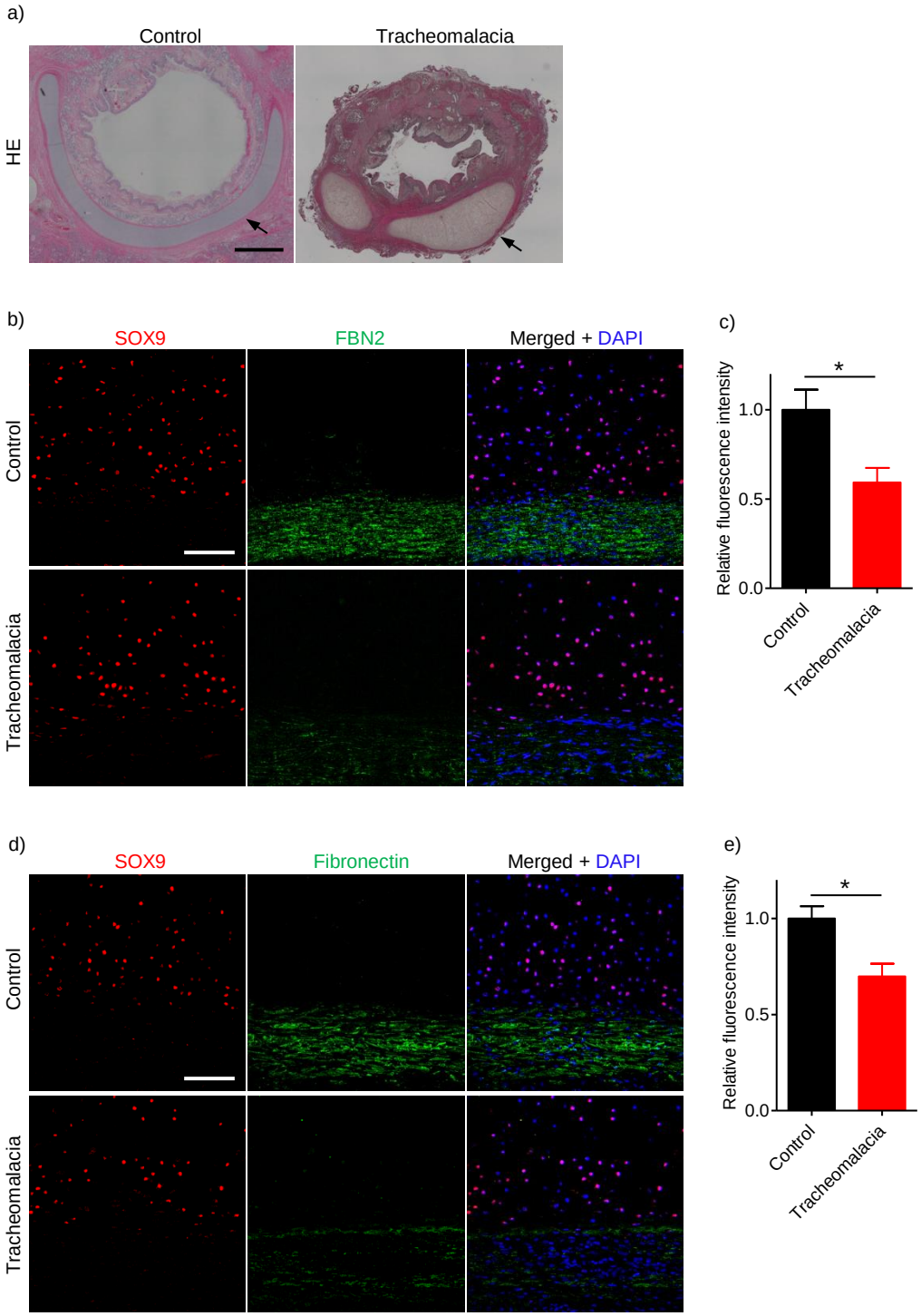

Yin et al., Fig. 8.

Supplemental Figure Legends

Figure S1: *Fbn2*$^{T2547A/T2547A}$ mice exhibit a lower body weight.

(A) Representative gross morphology of P7 WT (n=16) and mutants (n=16). **(B)** Quantification of body weight of P7 WT (n=16) and mutants (n=16). **(C)** Representative gross morphology of 5-months-old WT (n=6) and mutants (n=6). **(D)** Quantification of ratios of tracheal tube length to nose to anus length. **(E)** Quantification of respiratory rates of P60 WT (n=6) and mutants (n=6). ***P* < 0.05; ****P* < 0.01; NS, not significant; Unpaired Student's *t*-test, mean ± s.d.

Figure S2: *Fbn2*$^{-/-}$ mice exhibit tracheal tube formation defects.

(A) Representative image of ventral view of wholemount tracheas stained with alcian blue from P14 WT (n=6) and *Fbn2*$^{-/-}$ mice (n=6). Double-sided arrows indicate tracheal tube length. Arrows point to tracheal cartilage rings. **(B)** Quantification of P14 WT (n=6) and *Fbn2*$^{-/-}$ (n=6) tracheal tube length. **(C)** Quantification of the number of P14 WT (n=6) and *Fbn2*$^{-/-}$ (n=6) tracheal cartilage rings. **(D)** Representative images of dorsal views of wholemount tracheas stained for αSMA (red) from P7 WT (n=6) and *Fbn2*$^{-/-}$ mice (n=6). **(E)** Quantification of P7 WT (n=6) and *Fbn2*$^{-/-}$ (n=6) tracheal SM cell orientation. Scale bars: 2000 μm (A), 50 μm (D). ****P* < 0.01; Unpaired Student's *t*-test, mean ± s.d.

Figure S3: *Fbn2*$^{T2547A/T2547A}$ limbs exhibit fusion of the digits.

(A) Representative images of wholemount hindlimbs stained with alcian blue from E13.5 WT (n=6) and *Fbn2*$^{T2547A/T2547A}$ (n=6) embryos. The arrow points to digit fusion. **(B)** Representative images of the hindlimbs from P6 (n=6) and 5-months-old (n=6) WT and *Fbn2*$^{T2547A/T2547A}$ (n=6 at P6, n=6 at 5 months) mice. Arrows point to digit fusion. **(C)** Representative images of wholemount hindlimbs stained with alcian blue and alizarin red from P6 WT (n=6) and *Fbn2*$^{T2547A/T2547A}$ (n=6) mice. The arrow points to digit fusion. **(D)** Representative images of wholemount forelimbs stained with alcian blue from E13.5 WT (n=6) and *Fbn2*$^{T2547A/T2547A}$ (n=6) embryos. **(E)** Representative images of the forelimbs from P6 (n=6) and 5-months-old (n=6) WT and *Fbn2*$^{T2547A/T2547A}$ (n=6 at P6, n=6 at 5 months) mice. **(F)** Representative images of wholemount forelimbs stained with alcian blue and alizarin red from P6 WT (n=6) and *Fbn2*$^{T2547A/T2547A}$ (n=6) mice. Scale bars: 2000 μm (B, C, E, F), 1000 μm (A, D).

Figure S4: *Fbn2*$^{T2547A/T2547A}$ mice exhibit cartilage formation defects in intrapulmonary airways.

(A) Immunostaining for SOX9 (green) in ventral views of E16.5 WT (n=6) and *Fbn2*$^{T2547A/T2547A}$ (n=6) intrapulmonary airways. Arrows point to cartilage rings. **(B)** Quantification of the relative number of intact cartilage rings in intrapulmonary airways in E16.5 WT (n=6) and *Fbn2*$^{T2547A/T2547A}$ (n=6) mice. **(C)** Representative images of ventral

views of intrapulmonary airways stained with alcian blue from P0 WT (n=6) and *Fbn2*$^{T2547A/T2547A}$ (n=6) mice. Arrows point to cartilage rings. **(D)** Quantification of the relative number of intact cartilage rings in intrapulmonary airways in P0 WT (n=6) and *Fbn2*$^{T2547A/T2547A}$ (n=6) mice. Scale bars: 1000 μm (C), 500 μm (A). ****P* < 0.01; Unpaired Student's *t*-test, mean ± s.d.

Figure S5: *Fbn2*$^{T2547A/T2547A}$ mice exhibit WT-like lung branching morphogenesis and alveologenesis.

(A) Immunostaining for SOX9 (green) in dorsal views of E14.5 WT (n=6) and *Fbn2*$^{T2547A/T2547A}$ (n=6) right cranial lung lobe. Arrows point to branch tips. **(B)** Quantification of the relative branch tip number of E14.5 WT (n=6) and *Fbn2*$^{T2547A/T2547A}$ (n=6) right cranial lung lobe. **(C)** Representative images of lung tissue sections stained with hematoxylin and eosin from WT (n=6) and *Fbn2*$^{T2547A/T2547A}$ mice (n=6) at several postnatal stages. **(D)** Quantification of the relative mean linear intercept of WT (n=6) and *Fbn2*$^{T2547A/T2547A}$ (n=6) lungs at several postnatal stages. Scale bars: 500 μm (A), 100 μm (C). NS, not significant; Unpaired Student's *t*-test, mean ± s.d.

Figure S6: *Fbn2*$^{T2547A/T2547A}$ lungs exhibit WT-like epithelial and mesenchymal cell differentiation.

(A) Immunostaining for acetylated alpha-Tubulin (multiciliated cells; green) and CC10 (club cells; red), and DAPI staining (blue) of P14 WT (n=6) and *Fbn2*$^{T2547A/T2547A}$ (n=6) lungs. **(B)** Quantification of CC10^{+} cells in 1 mm airway of P14 WT (n=6) and *Fbn2*$^{T2547A/T2547A}$ (n=6) lungs. **(C)** Quantification of acetylated alpha-Tubulin^{+} cells in 1 mm airway of P14 WT (n=6) and *Fbn2*$^{T2547A/T2547A}$ (n=6) lungs. **(D)** Immunostaining for SFTPC (alveolar type 2 cells; green) and RAGE (alveolar type 1 cells; red), and DAPI staining (blue) of P14 WT (n=6) and *Fbn2*$^{T2547A/T2547A}$ (n=6) lungs. **(E)** Quantification of SFTPC^{+} cell ratio of P14 WT (n=6) and *Fbn2*$^{T2547A/T2547A}$ (n=6) lungs. **(F)** Quantification of relative mean fluorescence intensity of RAGE immunostaining of P14 WT (n=6) and *Fbn2*$^{T2547A/T2547A}$ (n=6) lungs. **(G)** Immunostaining for PECAM (endothelial cells; green) and vimentin (fibroblasts; red), and DAPI staining (blue) of P14 WT (n=6) and *Fbn2*$^{T2547A/T2547A}$ (n=6) lungs. **(H)** Quantification of relative mean fluorescence intensity of PECAM immunostaining of P14 WT (n=6) and *Fbn2*$^{T2547A/T2547A}$ (n=6) lungs. **(I)** Quantification of relative mean fluorescence intensity of vimentin immunostaining of P14 WT (n=6) and *Fbn2*$^{T2547A/T2547A}$ (n=6) lungs. Scale bars: 100 μm. NS, not significant; Unpaired Student's *t*-test, mean ± s.d.

Figure S7: *Fbn2*$^{T2547A/+}$ mice exhibit WT-like tracheal cartilage formation, SM cell orientation and limb patterning.

(A) Representative images of ventral views of wholemount tracheas stained with alcian blue from P0 WT (n=6) and *Fbn2*$^{T2547A/+}$ (n=6) mice. Double-sided arrows indicate tracheal tube length. Arrows point to tracheal cartilage rings. **(B)** Quantification of P0 WT (n=6) and

Fbn2$^{T2547A/+}$ (n=6) tracheal tube length. **(C)** Quantification of the number of P0 WT (n=6) and *Fbn2* $^{T2547A+}$ (n=6) tracheal cartilage rings. **(D)** Immunostaining for αSMA (red) and DAPI staining (blue) in dorsal views of P0 WT (n=6) and *Fbn2*$^{T2547A/+}$ (n=6) tracheas. **(E)** Quantification of P0 WT (n=6) and *Fbn2*$^{T2547A/+}$ (n=6) tracheal SM cell orientation. **(F)** Representative images of wholemount hindlimbs stained with alcian blue and alizarin red from P6 WT (n=6) and *Fbn2*$^{T2547A/+}$ (n=6) mice. Scale bars: 2000 μm (F), 1000 μm (A), 20 μm (D). NS, not significant; Unpaired Student's *t*-test, mean ± s.d.

Figure S8: *Fbn2* mRNA expression is observed in chondroblasts and SM in tracheas.

(A) mRNA in situ hybridization for *Fbn2* expression in transverse sections of E14.5 WT tracheas (n=6). Asterisks indicate chondroblasts. **(B)** mRNA in situ hybridization for *Fbn2* expression in transverse sections of ventral parts of E16.5 WT tracheas (n=6). Asterisks indicate chondrocytes based on position and shape. **(C)** mRNA in situ hybridization for *Fbn2* expression in transverse sections of dorsal parts of E16.5 WT tracheas (n=6). Arrow points to SM cells based on position and shape. Scale bars: 100 μm. Te, Tracheal epithelium.

Figure S9: *Fbn2*$^{T2547A/T2547A}$ tracheas exhibit reduced AGC1 and COL2A1 protein levels.

(A) Immunostaining for AGC1 (red) and DAPI staining (blue) of transverse sections of E15.5 WT (n=6) and *Fbn2*$^{T2547A/T2547A}$ (n=6) tracheas. **(B)** Quantification of mean fluorescence intensity of AGC1 immunostaining in E15.5 WT (n=6) and *Fbn2*$^{T2547A/T2547A}$ (n=6) tracheas. **(C)** Immunostaining for COL2A1 (green) and DAPI staining (blue) of transverse sections of E15.5 WT (n=6) and *Fbn2*$^{T2547A/T2547A}$ (n=6) tracheas. **(D)** Quantification of mean fluorescence intensity of COL2A1 immunostaining in E15.5 WT (n=6) and *Fbn2*$^{T2547A/T2547A}$ (n=6) tracheas. Scale bars: 20 μm. ***P* < 0.01; Unpaired Student's *t*-test, mean ± s.d.

Figure S10: *Fbn2*$^{T2547A/T2547A}$ tracheas display no obvious defects in SM cell or chondroblast proliferation or apoptosis.

(A) Immunostaining for αSMA (red) and cleaved caspase-3 (CASP3, green), and DAPI staining (blue) of transverse sections of E14.5 WT (n=6) and *Fbn2*$^{T2547A/T2547A}$ (n=6) tracheas. **(B)** Immunostaining for CASP3 (green) and DAPI staining (blue) of P5 WT lung tissue sections (n=5) as a positive control. Arrows point to apoptotic cells. **(C)** Percentage of αSMA$^+$ cells that are CASP3$^+$. **(D)** Immunostaining for PCNA (red) and SOX9 (green), and DAPI staining (blue) of transverse sections of E14.5 WT (n=6) and *Fbn2*$^{T2547A/T2547A}$ (n=6) tracheas. **(E)** Percentage of SOX9$^+$ cells that are PCNA$^+$. **(F)** Immunostaining for αSMA (red) and Ki67 (green), and DAPI staining (blue) of transverse sections of E14.5 WT (n=6) and *Fbn2*$^{T2547A/T2547A}$ (n=6) tracheas. **(G)** Percentage of αSMA$^+$ cells that are Ki67$^+$. Scale bars: 100 μm (A, B, D), 50 μm (F). NS, not significant; Unpaired Student's *t*-test, mean ± s.d.

Figure S11: Isolated *Fbn2*$^{T2547A/T2547A}$ tracheal chondrocytes exhibit defects in chondrogenesis.

(A) Alcian blue staining of isolated chondrocytes from E14.5 WT (n=6) and *Fbn2*$^{T2547A/T2547A}$ (n=6) tracheas after 9 days of culture. Arrows point to condensed chondrocytes. **(B)** Quantification of relative alcian blue areas in WT (6) and *Fbn2*$^{T2547A/T2547A}$ (6) cultures. Scale bars: 100 μm. ****P* < 0.01; Unpaired Student's *t*-test, mean ± s.d.

Figure S12: *Fbn2*$^{T2547A/T2547A}$ mice display no obvious defects in tracheal epithelial cell proliferation or mitotic spindle orientation.

(A) Immunostaining for CDH1 (red) and PH3 (green), and DAPI staining (blue) of transverse sections of E15.5 WT (n=7) and *Fbn2*$^{T2547A/T2547A}$ (n=7) tracheas. **(B)** Quantification of the mitotic spindle angle of E15.5 WT (n=7) and *Fbn2*$^{T2547A/T2547A}$ (n=7) dividing epithelial cells. 35 cells were analyzed per animal. **(C)** Immunostaining for CDH1 (red) and Ki67 (green), and DAPI staining (blue) of transverse sections of E15.5 WT (n=7) and *Fbn2*$^{T2547A/T2547A}$ (n=7) tracheas. **(D)** Percentage of CDH1^{+} cells that are Ki67^{+}. **(E)** RT–qPCR analysis of *Fgf10* expression in E14.5 WT (n=6) and *Fbn2*$^{T2547A/T2547A}$ (n=6) tracheas. Scale bars: 50 μm (C), 5 μm (A). NS, not significant; Unpaired Student's *t*-test, mean ± s.d.

Figure S13: *Fbn2*$^{T2547A/T2547A}$ mice display no obvious defects in esophageal elongation or esophageal SM cell orientation.

(A) Immunostaining for αSMA (red) and FBN2 (green), and DAPI staining (blue) of transverse sections of E13.5 WT esophagi (n=5). **(B)** Representative images of P0 WT (n=11) and *Fbn2*$^{T2547A/T2547A}$ (n=11) esophagi. Double-sided arrows indicate esophageal length. (**C**) Quantification of P0 WT (n=11) and *Fbn2*$^{T2547A/T2547A}$ (n=11) esophageal length. **(D)** Immunostaining for αSMA (red) in E14.5 WT (n=7) and *Fbn2*$^{T2547A/T2547A}$ (n=7) esophagi. **(E)** Immunostaining for αSMA (red) and DAPI staining (blue) in E14.5 WT (n=7) and *Fbn2*$^{T2547A/T2547A}$ (n=7) esophagi. **(F)** Quantification of E14.5 WT (n=7) and *Fbn2*$^{T2547A/T2547A}$ (n=7) esophageal SM cell orientation. **(G)** Immunostaining for αSMA (red) and Tropoelastin (green), and DAPI staining (blue) in E14.5 WT (n=7) and *Fbn2*$^{T2547A/T2547A}$ (n=7) esophagi. **(H, I)** Quantification of elastic fiber orientation (H) and short elastic fibers (I) around SM cells in E14.5 WT (n=7) and *Fbn2*$^{T2547A/T2547A}$ (n=7) esophagi. **(J)** RT–qPCR analysis of *Fbn1* expression in E14.5 WT esophagi (n=3). Scale bars: 1 mm (B), 50 μm (A, D), 20 μm (E, G). NS, not significant; Unpaired Student's *t*-test, mean ± s.d. A, Anterior; P, Posterior.

Figure S14: *Fbn2* modulates elastic fiber formation and Fibronectin accumulation in adult tracheas.

(A) Dorsal views of αSMA (red) and Tropoelastin (green) immunostaining and DAPI staining (blue) of P70 WT (n=6) and *Fbn2*$^{T2547A/T2547A}$ (n=6) tracheas. Arrows point to short elastic fibers. **B, C)** Quantification of elastic fiber orientation **B)** and short elastic fibers **C)** around SM cells in P70 WT (n=6) and *Fbn2*$^{T2547A/T2547A}$ (n=6) tracheas. **(D)** Western blotting for Fibronectin and GAPDH in P70 WT (n=5) and *Fbn2*$^{T2547A/T2547A}$ (n=5) tracheas. **(E)** Quantification of relative levels of Fibronectin in P70 WT (n=5) and *Fbn2*$^{T2547A/T2547A}$ (n=5) tracheas. **(F)** Western blotting for Elastin and GAPDH in P70 WT (n=5) and *Fbn2*$^{T2547A/T2547A}$

(n=5) tracheas. **(G)** Quantification of relative levels of Elastin in P70 WT (n=5) and *Fbn2*$^{T2547A/T2547A}$ (n=5) tracheas. Scale bars: 20 μm. ***P* < 0.05; ****P* < 0.01; NS, not significant; Unpaired Student's *t*-test, mean ± s.d.

Figure S15: *Fbn2*$^{T2547A/T2547A}$ mice exhibit WT-like mRNA expression levels of *Mmp2* in esophagi, and potential *Mmp2* and *Mmp9* regulators in tracheas.

(A) RT–qPCR analysis of *Mmp2* expression in E14.5 WT (n=6) and *Fbn2*$^{T2547A/T2547A}$ (n=6) esophagi. **(B)** RT–qPCR analysis of *Nfkb1*, *Nfkb2*, *Rela*, *Jun* and *Fos* expression in E14.5 WT (n=6) and *Fbn2*$^{T2547A/T2547A}$ (n=6) tracheas. **(C)** RT–qPCR analysis of *Atf2* and *Hspb1* expression in E14.5 WT (n=6) and *Fbn2*$^{T2547A/T2547A}$ (n=6) tracheas. NS, not significant; Unpaired Student's t-test, mean ± s.d.

Figure S16: *Fbn2*$^{T2547A/T2547A}$ mice exhibit increased levels of phosphorylated p38 in tracheal SM cells and WT-like levels of phosphorylated p38 in esophagi.

(A) Immunostaining for αSMA (red) and phosphorylated p38 (P-p38) (green), and DAPI staining (blue) of transverse sections of E15.5 WT (n=6) and *Fbn2*$^{T2547A/T2547A}$ (n=6) tracheas. **(B)** Percentage of αSMA^{+} cells that are P-p38^{+}. **(C)** Western blotting for P-p38, total p38 and GAPDH in P7 WT (n=6) and *Fbn2*$^{T2547A/T2547A}$ (n=6) esophagi. **(D)** Quantification of relative levels of P-p38 in P7 WT (n=6) and *Fbn2*$^{T2547A/T2547A}$ (n=6) esophagi. Scale bars: 50 μm. ***P* < 0.05; ****P* < 0.01; Unpaired Student's *t*-test, mean ± s.d.

Figure S17: Fibronectin localizes in peripheral regions of the tracheal cartilage.

Immunostaining for Fibronectin (green) and SOX9 (red), and DAPI staining (blue) of transverse sections of WT tracheas (n=5) mostly in cartilage regions, at embryonic and postnatal stages. Scale bars: 50 μm.

Supplemental table 1: qPCR data. mRNA expression levels were examined by RT-qPCR; Ct values listed.

Figure 2c

a

Sample Name	Gene Name	Ct mean
E12.5 WT	*Fbn2*	27.32
E12.5 *Fbn2*$^{T2547A/T2547A}$	*Fbn2*	28.18
E12.5 WT	*Actb*	23.66
E12.5 *Fbn2*$^{T2547A/T2547A}$	*Actb*	23.02

Figure 5h

b

Sample Name	Gene Name	Ct mean
E14.5 WT	*Fibronectin*	29.19
E14.5 *Fbn2*$^{T2547A/T2547A}$	*Fibronectin*	28.92
E14.5 WT	*Actb*	25.34
E14.5 *Fbn2*$^{T2547A/T2547A}$	*Actb*	25.38

Figure 6a

c

Sample Name	Gene Name	Ct mean
E14.5 WT	*Mmp2*	22.18
E14.5 *Fbn2*$^{T2547A/T2547A}$	*Mmp2*	21.74
E14.5 WT	*Mmp9*	29.25
E14.5 *Fbn2*$^{T2547A/T2547A}$	*Mmp9*	27.54
E14.5 WT	*Actb*	18.65
E14.5 *Fbn2*$^{T2547A/T2547A}$	*Actb*	19.12
P7 WT	*Mmp2*	24.47
P7 *Fbn2*$^{T2547A/T2547A}$	*Mmp2*	22.08
P7 WT	*Mmp9*	31.20
P7 *Fbn2*$^{T2547A/T2547A}$	*Mmp9*	28.27
P7 WT	*Actb*	20.18
P7 *Fbn2*$^{T2547A/T2547A}$	*Actb*	19.25

Figure 7c

d

Sample Name	Gene Name	Ct mean
E14.5 WT +DMSO	*Mmp2*	23.42
E14.5 *Fbn2*$^{T2547A/T2547A}$ + DMSO	*Mmp2*	22.40
E14.5 *Fbn2*$^{T2547A/T2547A}$ + SB203580	*Mmp2*	22.91
E14.5 WT +DMSO	*Mmp9*	30.95
E14.5 *Fbn2*$^{T2547A/T2547A}$ + DMSO	*Mmp9*	28.36

E14.5 *Fbn2*$^{T2547A/T2547A}$ + SB203580	*Mmp9*	29.21
E14.5 WT +DMSO	*Actb*	20.07
E14.5 *Fbn2*$^{T2547A/T2547A}$ + DMSO	*Actb*	19.62
E14.5 *Fbn2*$^{T2547A/T2547A}$ + SB203580	*Actb*	19.71

Figure S12E

e

Sample Name	Gene Name	Ct mean
E14.5 WT	*Fgf10*	30.42
E14.5 *Fbn2*$^{T2547A/T2547A}$	*Fgf10*	30.60
E14.5 WT	*Actb*	24.20
E14.5 *Fbn2*$^{T2547A/T2547A}$	*Actb*	24.22

Figure S13J

f

Sample Name	Gene Name	Ct mean
E14.5 WT	*Fbn1*	28.03
E14.5 WT	*Actb*	23.39

Figure S15A

g

Sample Name	Gene Name	Ct mean
E14.5 WT	*Mmp2*	28.13
E14.5 *Fbn2*$^{T2547A/T2547A}$	*Mmp2*	27.56
E14.5 WT	*Mmp9*	N/A
E14.5 *Fbn2*$^{T2547A/T2547A}$	*Mmp9*	N/A
E14.5 WT	*Actb*	23.42
E14.5 *Fbn2*$^{T2547A/T2547A}$	*Actb*	22.47

Figure S15B

h

Sample Name	Gene Name	Ct mean
E14.5 WT	*Nfkb1*	30.27
E14.5 *Fbn2*$^{T2547A/T2547A}$	*Nfkb1*	29.93
E14.5 WT	*Nfkb2*	30.67
E14.5 *Fbn2*$^{T2547A/T2547A}$	*Nfkb2*	30.67
E14.5 WT	*Rela*	31.89
E14.5 *Fbn2*$^{T2547A/T2547A}$	*Rela*	31.57
E14.5 WT	*Jun*	26.70
E14.5 *Fbn2*$^{T2547A/T2547A}$	*Jun*	27.21
E14.5 WT	*Fos*	27.12
E14.5 *Fbn2*$^{T2547A/T2547A}$	*Fos*	27.74
E14.5 WT	*Actb*	23.93
E14.5 *Fbn2*$^{T2547A/T2547A}$	*Actb*	24.02

Figure S15C

i

Sample Name	Gene Name	Ct mean
E14.5 WT	*Atf2*	29.67
E14.5 *Fbn2*$^{T2547A/T2547A}$	*Atf2*	28.84
E14.5 WT	*Hspb1*	30.64
E14.5 *Fbn2*$^{T2547A/T2547A}$	*Hspb1*	30.44
E14.5 WT	*Actb*	23.92
E14.5 *Fbn2*$^{T2547A/T2547A}$	*Actb*	23.42

Supplemental table 2: Healthy control and tracheomalacia patient characteristics.

Samples	Age (day, month or year)	Gender	History of large airway disease	Other conditions
Control 1	1 day	Female	None	Premature
Control 2	1 day	Female	None	None
Control 3	14 days	Male	None	Premature
Control 4	UK	UK	None	None
Control 5	2 days	Female	None	None
Tracheomalacia 1	UK	UK	Tracheomalacia	None
Tracheomalacia 3	10 months	Female	Tracheomalacia	None
Tracheomalacia 4	7 months	Male	Tracheomalacia	None
Tracheomalacia 6	8 years	Female	Tracheomalacia	None
Tracheomalacia 7	2 years	Female	Tracheomalacia	None
Tracheomalacia 8	11 months	Male	Tracheomalacia	None
Tracheomalacia 9	9 months	Male	Tracheomalacia	None

UK: Data not available.

Supplementary movie 1

Compared to WT tracheas (n=6), *Fbn2*$^{T2547A/T2547A}$ tracheas (n=6) exhibit longer contracting times and reduced amplitude of spontaneous contractions at E13.5.

Figure S1

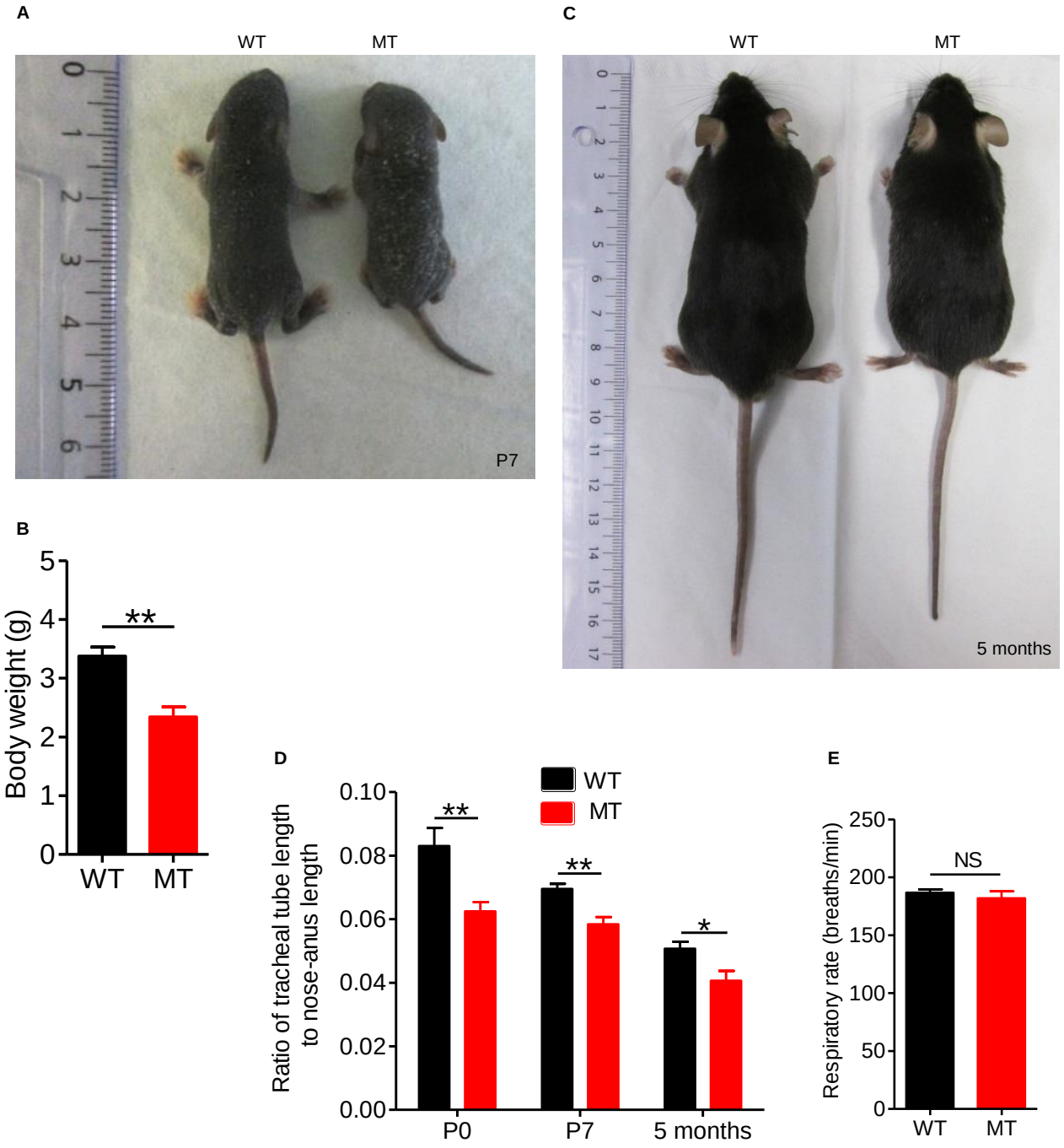
A
WT
MT
P7
C
WT
MT
5 months
B
Body weight (g)
**
WT
MT
D
Ratio of tracheal tube length to nose-anus length
WT
MT
**
**
*
P0
P7
5 months
E
Respiratory rate (breaths/min)
NS
WT
MT

Figure S2

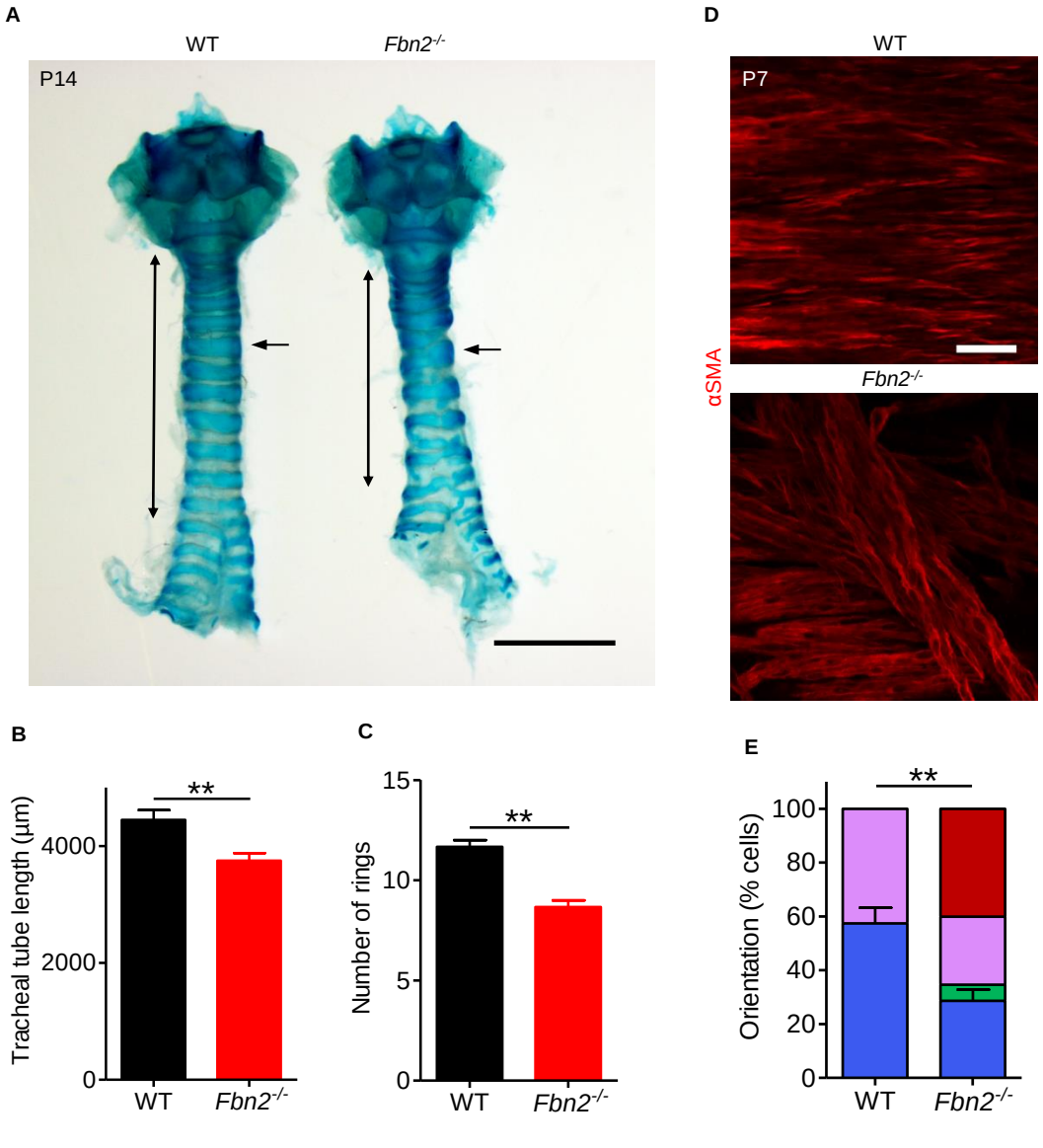
A
WT
Fbn2-/-
P14
D
WT
P7
αSMA
Fbn2-/-
B
Tracheal tube length (μm)
4000
2000
0
**
WT
Fbn2-/-
C
Number of rings
15
10
5
0
**
WT
Fbn2-/-
E
Orientation (% cells)
100
80
60
40
20
0
**
WT
Fbn2-/-

Figure S3

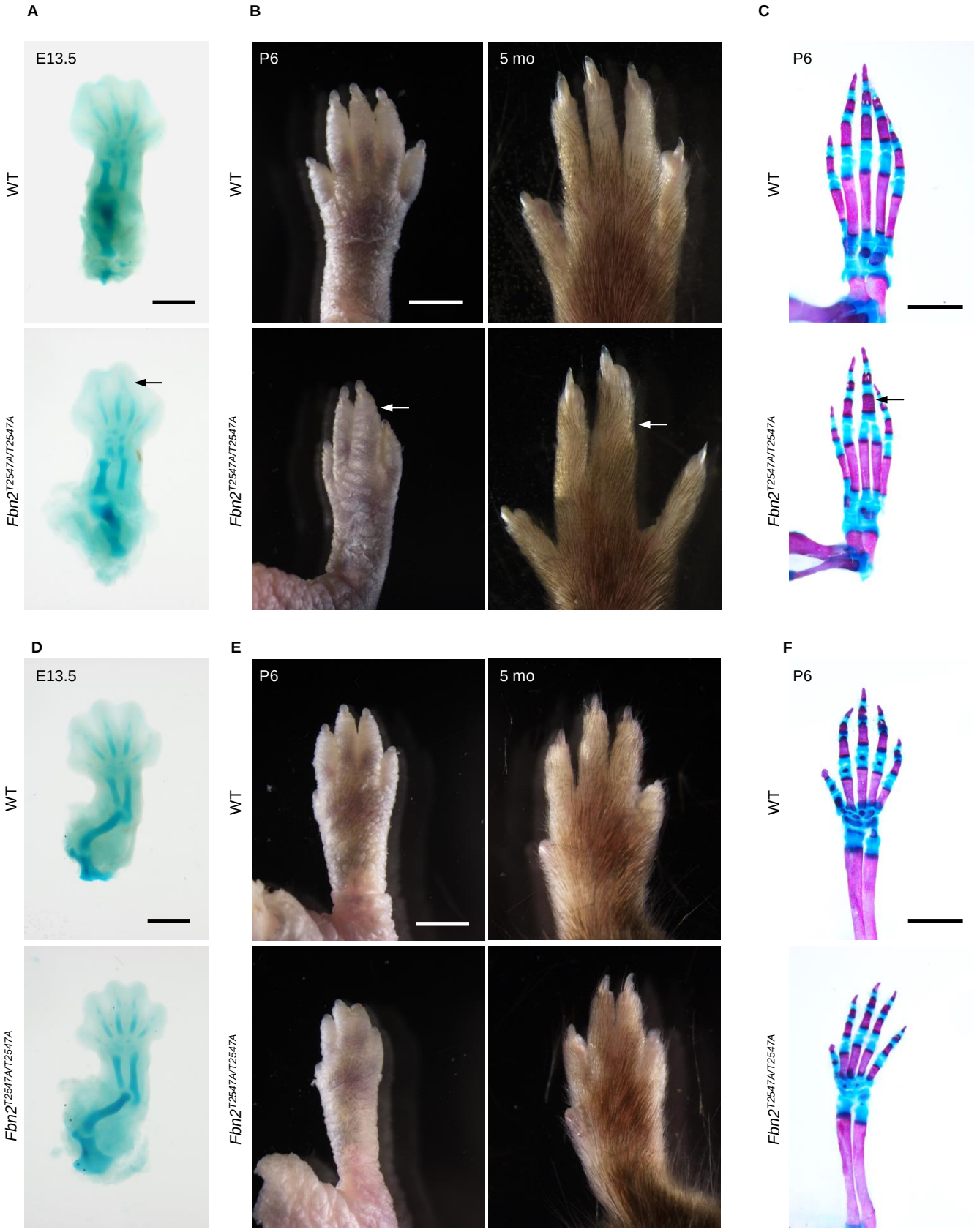
A
B
C
E13.5
P6
5 mo
P6
WT
Fbn2T2547A/T2547A
D
E
F
E13.5
P6
5 mo
P6
WT
Fbn2T2547A/T2547A

Figure S4

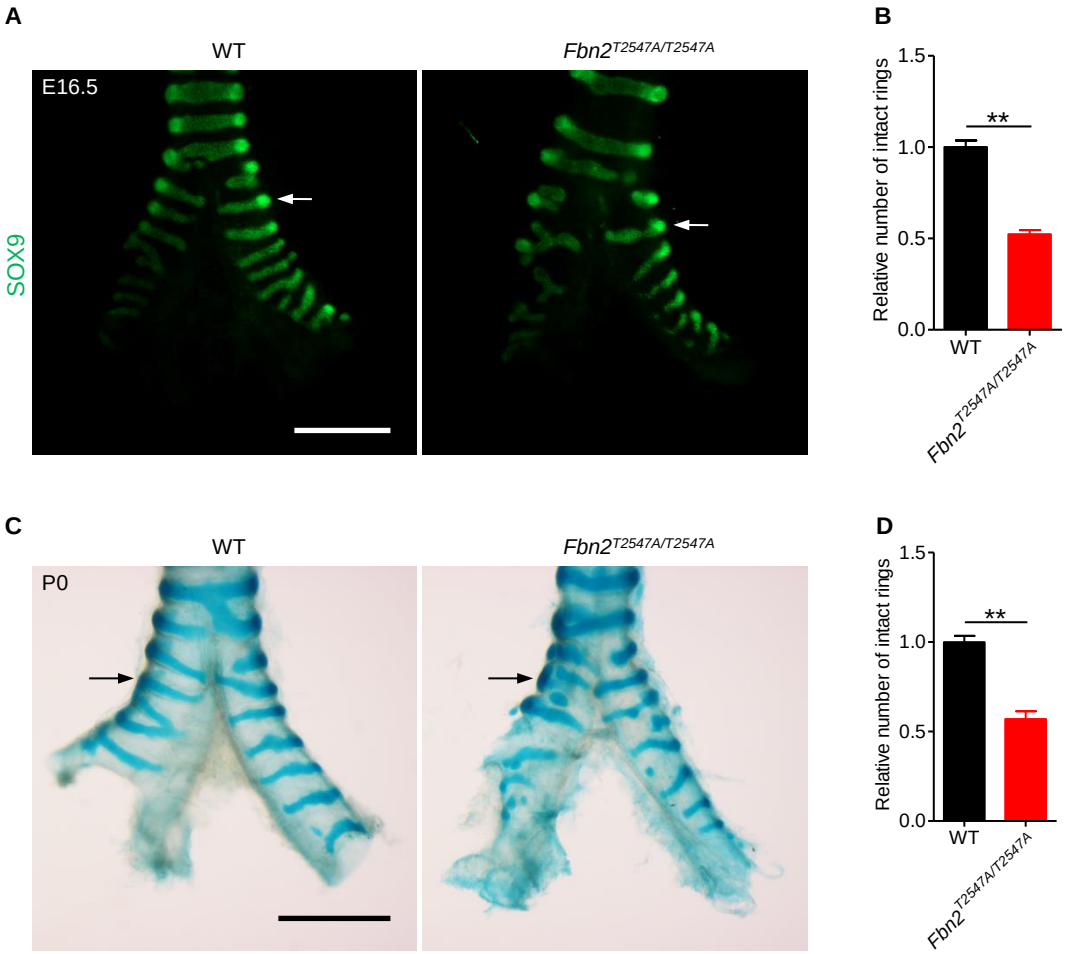
A
WT
Fbn2T2547A/T2547A
E16.5
SOX9
B
Relative number of intact rings
1.5
1.0
0.5
0.0
**
WT
Fbn2T2547A/T2547A
C
WT
Fbn2T2547A/T2547A
P0
D
Relative number of intact rings
1.5
1.0
0.5
0.0
**
WT
Fbn2T2547A/T2547A

Figure S5

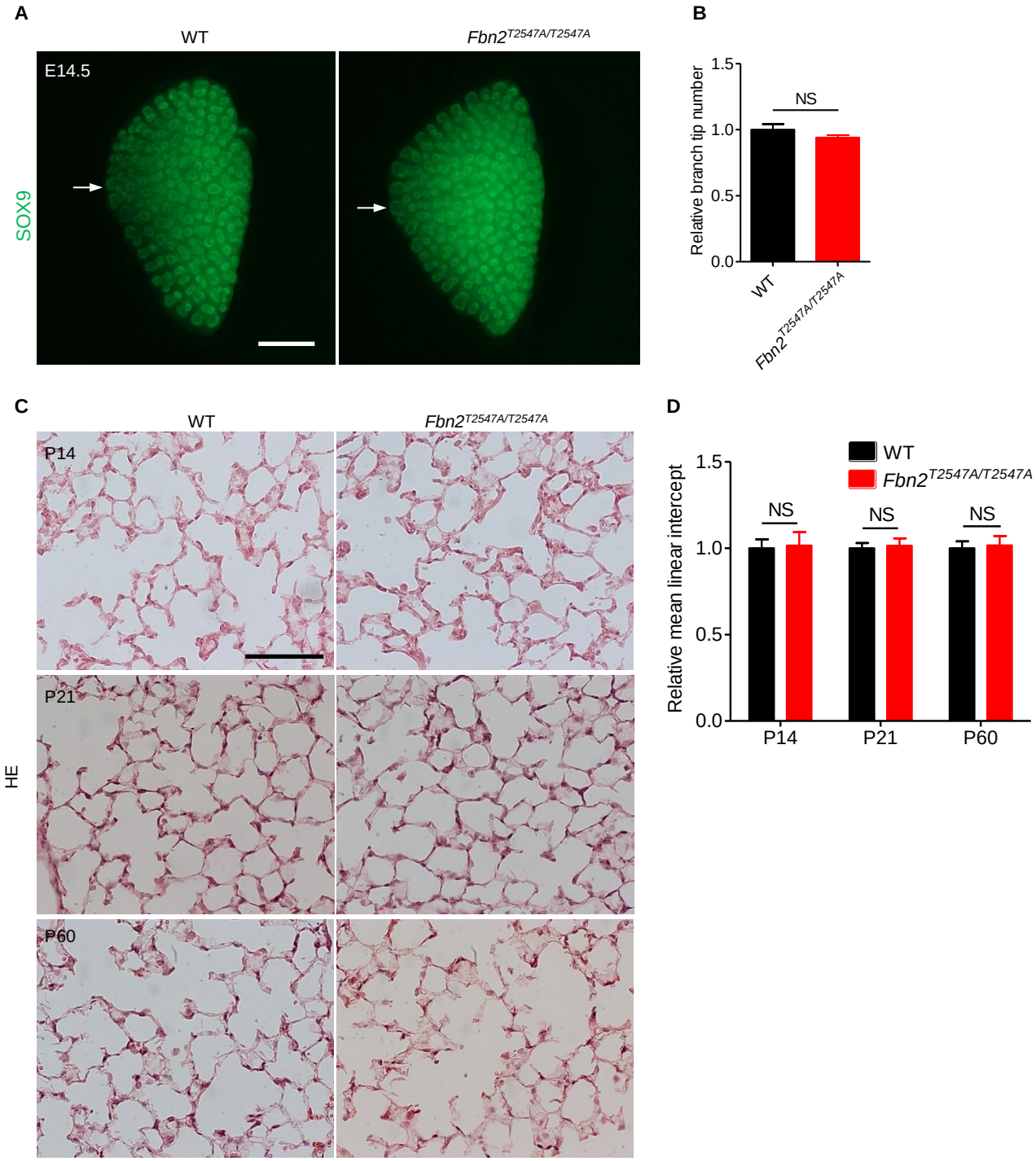
A
WT
Fbn2T2547A/T2547A
E14.5
SOX9
B
Relative branch tip number
1.5
1.0
0.5
0.0
NS
WT
Fbn2T2547A/T2547A
C
WT
Fbn2T2547A/T2547A
P14
P21
P60
HE
D
WT
Fbn2T2547A/T2547A
Relative mean linear intercept
1.5
1.0
0.5
0.0
NS
NS
NS
P14
P21
P60

Figure S6

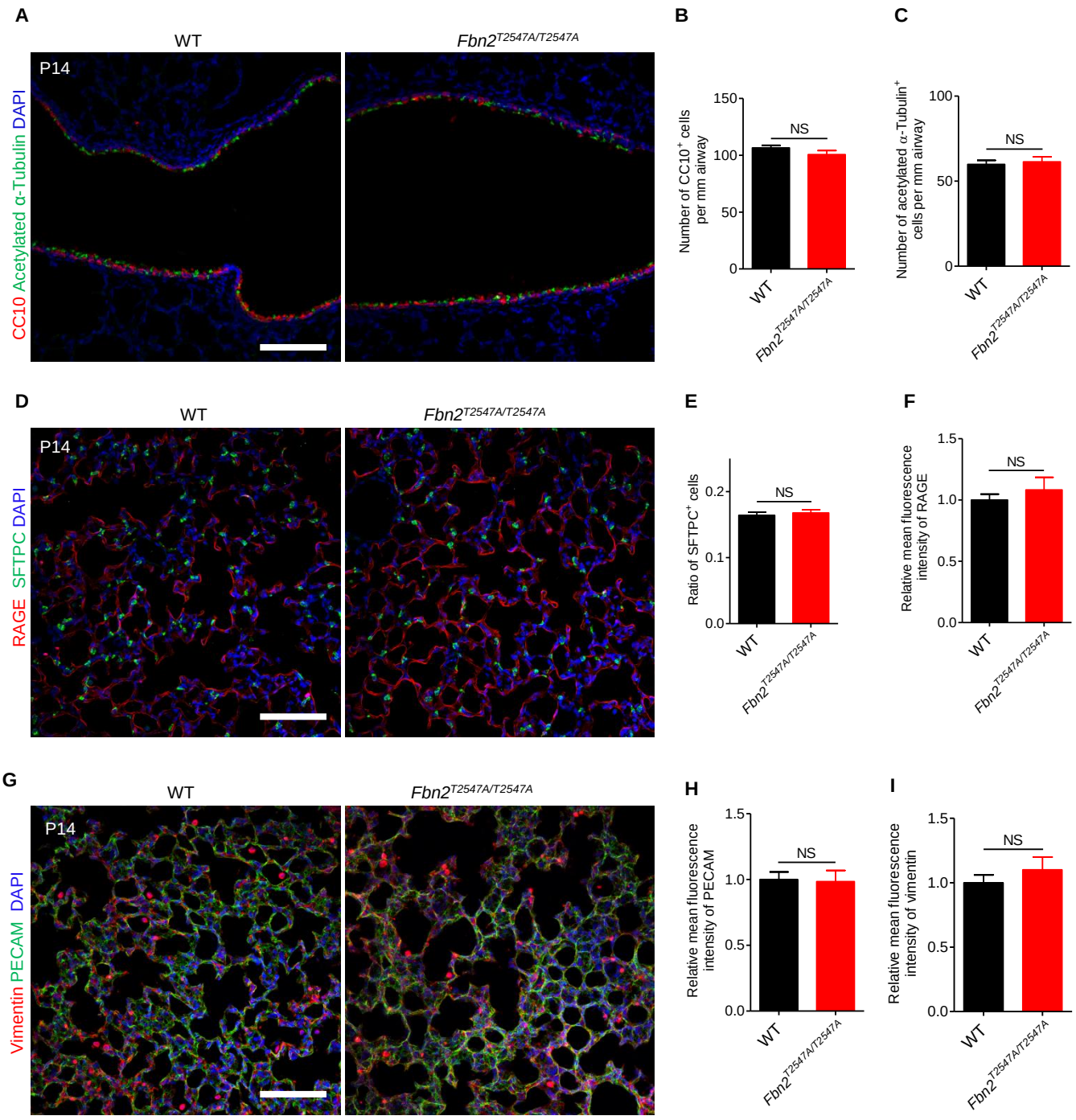
A
WT
Fbn2T2547A/T2547A
P14
CC10 Acetylated α-Tubulin DAPI
B
Number of CC10+ cells per mm airway
150
100
50
0
NS
WT
Fbn2T2547A/T2547A
C
Number of acetylated α-Tubulin+ cells per mm airway
100
50
0
NS
WT
Fbn2T2547A/T2547A
D
WT
Fbn2T2547A/T2547A
P14
RAGE SFTPC DAPI
E
Ratio of SFTPC+ cells
0.2
0.1
0.0
NS
WT
Fbn2T2547A/T2547A
F
Relative mean fluorescence intensity of RAGE
1.5
1.0
0.5
0.0
NS
WT
Fbn2T2547A/T2547A
G
WT
Fbn2T2547A/T2547A
P14
Vimentin PECAM DAPI
H
Relative mean fluorescence intensity of PECAM
1.5
1.0
0.5
0.0
NS
WT
Fbn2T2547A/T2547A
I
Relative mean fluorescence intensity of vimentin
1.5
1.0
0.5
0.0
NS
WT
Fbn2T2547A/T2547A

Figure S7

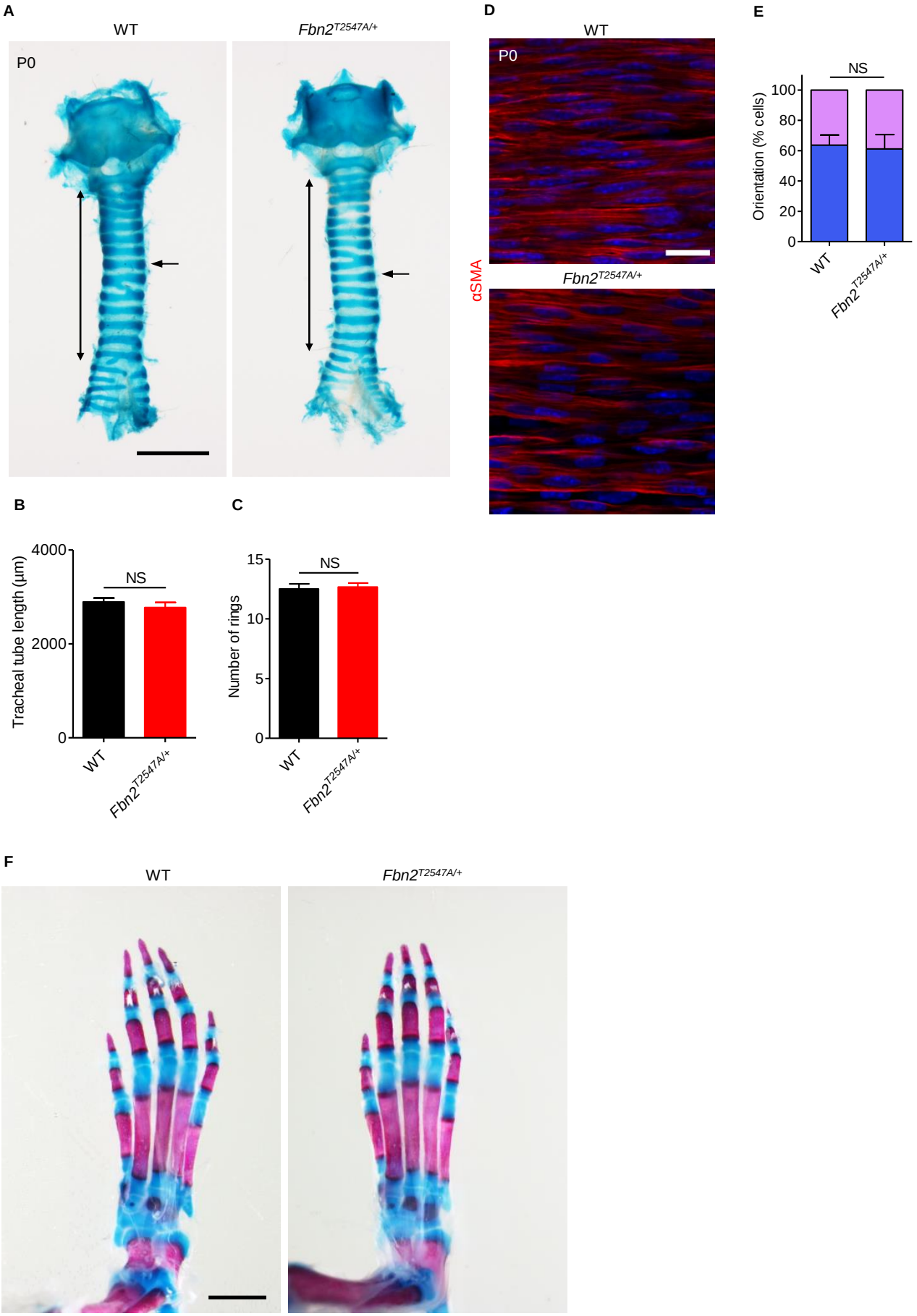
A
WT
Fbn2T2547A/+
P0
B
Tracheal tube length (µm)
4000
2000
0
NS
WT
Fbn2T2547A/+
C
Number of rings
15
10
5
0
NS
WT
Fbn2T2547A/+
D
WT
P0
αSMA
Fbn2T2547A/+
E
Orientation (% cells)
100
80
60
40
20
0
NS
WT
Fbn2T2547A/+
F
WT
Fbn2T2547A/+

Figure S8

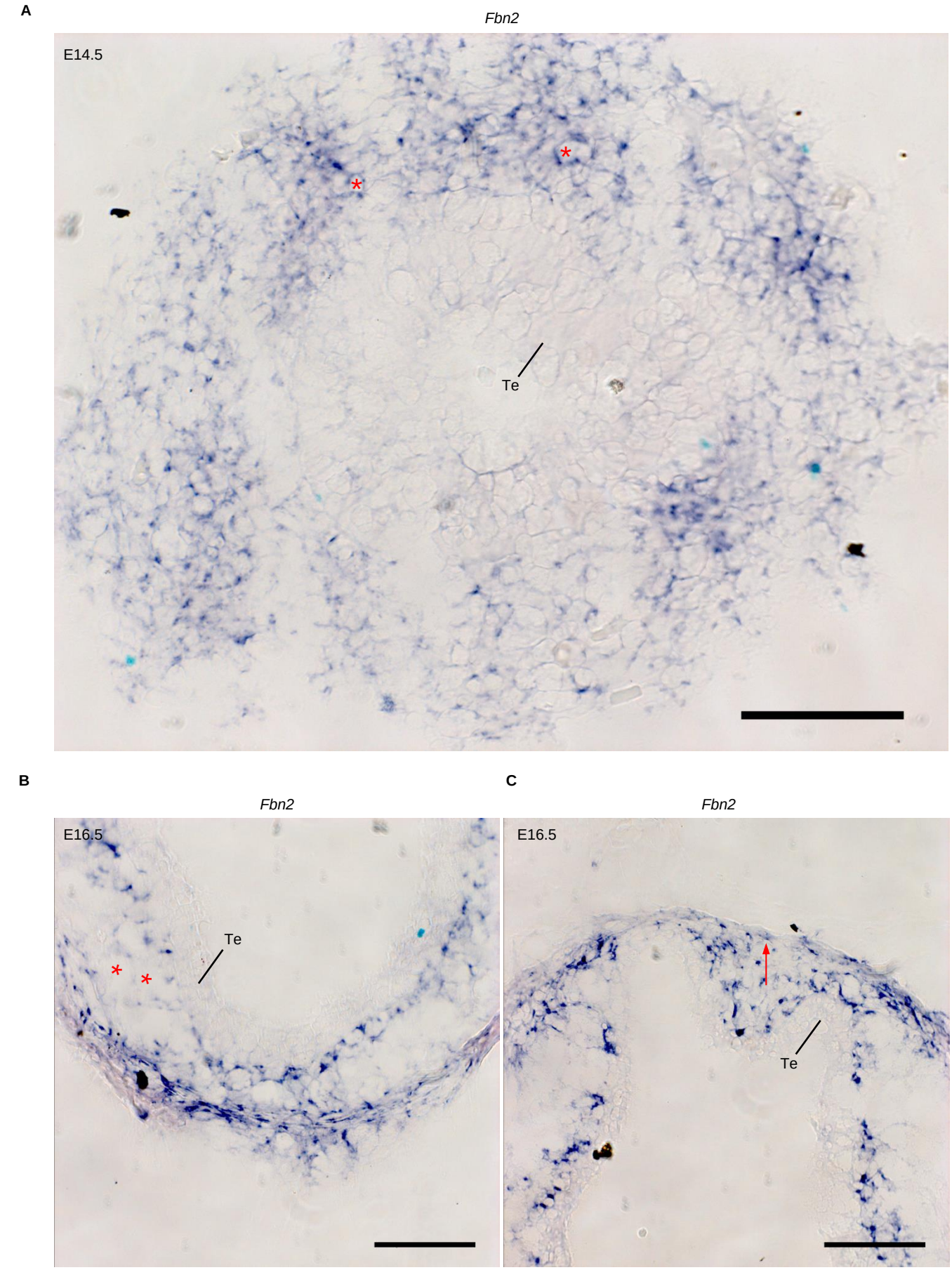

Figure S9

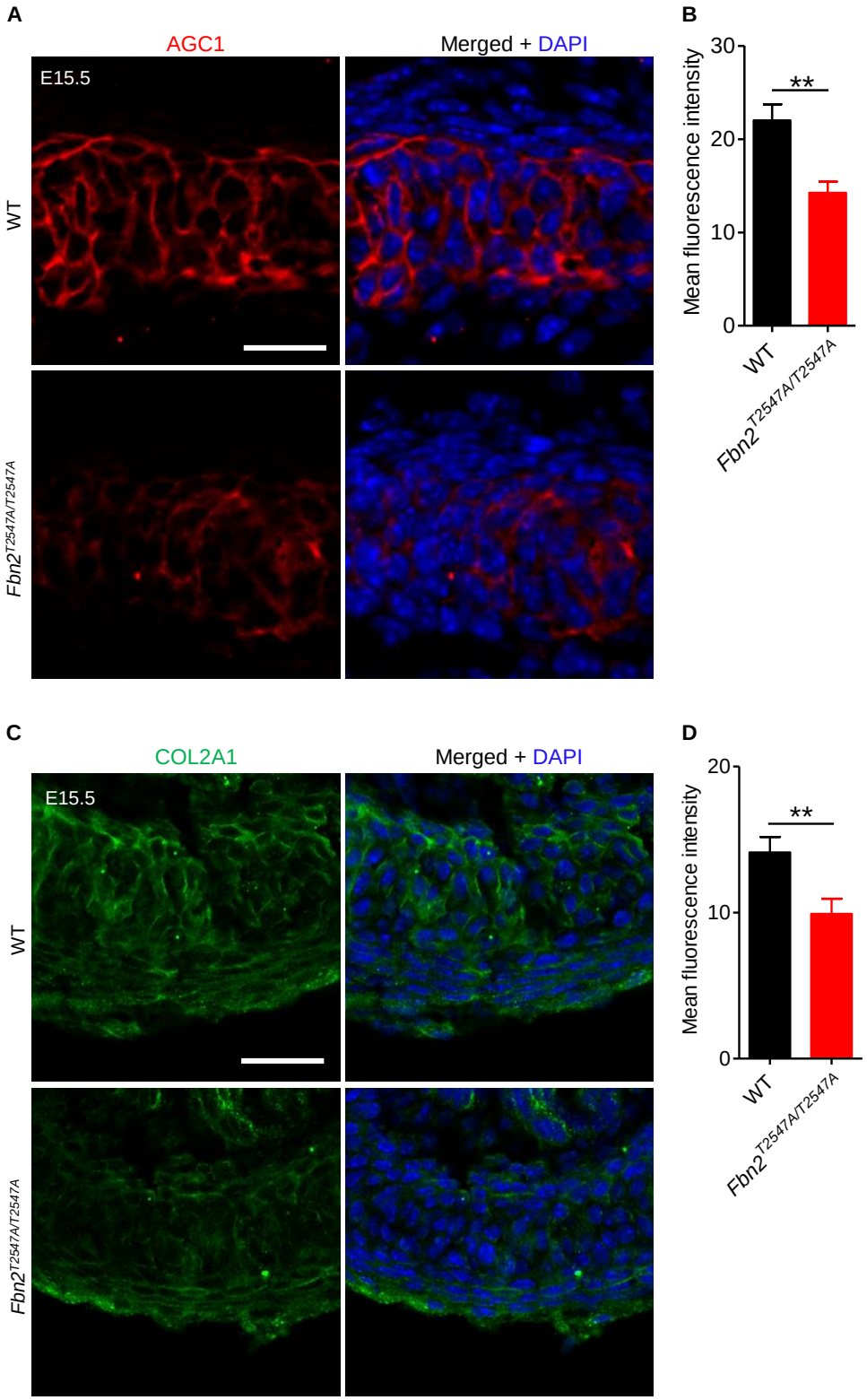
A
AGC1
Merged + DAPI
E15.5
WT
Fbn2T2547A/T2547A
B
Mean fluorescence intensity
30
20
10
0
**
WT
Fbn2T2547A/T2547A
C
COL2A1
Merged + DAPI
E15.5
WT
Fbn2T2547A/T2547A
D
Mean fluorescence intensity
20
10
0
**
WT
Fbn2T2547A/T2547A

Figure S10

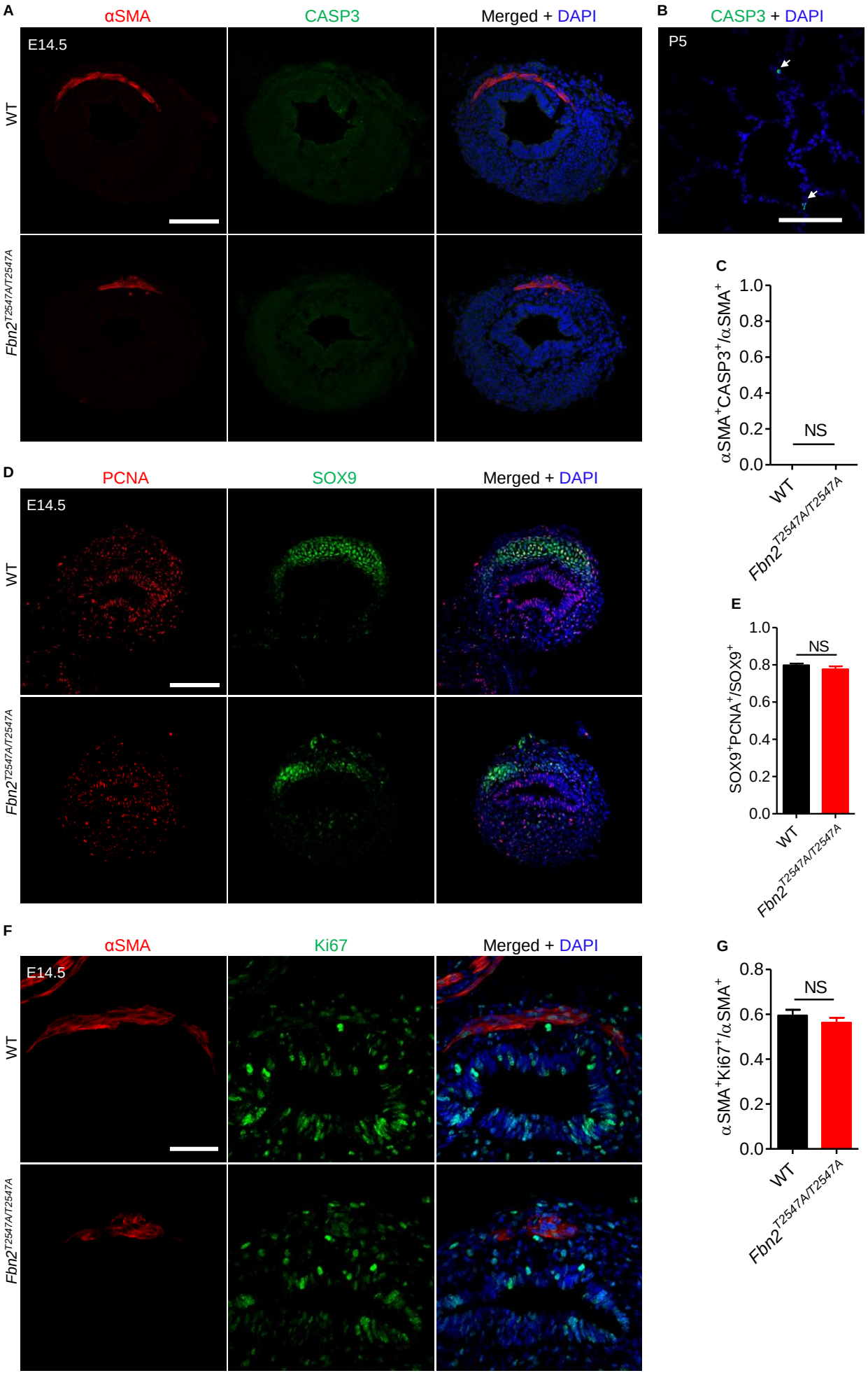
A
αSMA
CASP3
Merged + DAPI
E14.5
WT
Fbn2T2547A/T2547A
B
CASP3 + DAPI
P5
C
αSMA+CASP3+/αSMA+
1.0
0.8
0.6
0.4
0.2
0.0
NS
WT
Fbn2T2547A/T2547A
D
PCNA
SOX9
Merged + DAPI
E14.5
WT
Fbn2T2547A/T2547A
E
SOX9+PCNA+/SOX9+
1.0
0.8
0.6
0.4
0.2
0.0
NS
WT
Fbn2T2547A/T2547A
F
αSMA
Ki67
Merged + DAPI
E14.5
WT
Fbn2T2547A/T2547A
G
αSMA+Ki67+/αSMA+
0.8
0.6
0.4
0.2
0.0
NS
WT
Fbn2T2547A/T2547A

Figure S11

A

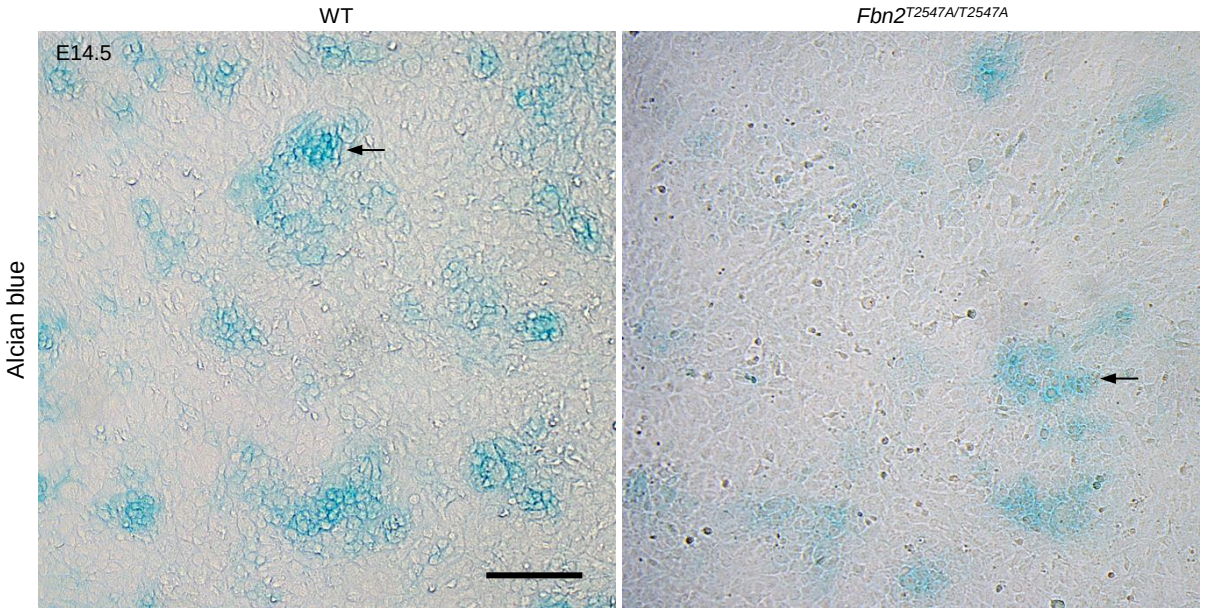

B

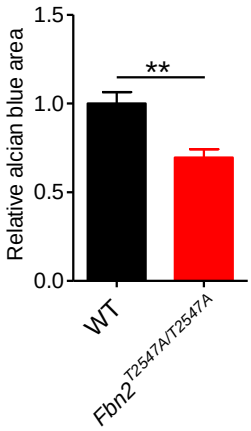

Figure S12

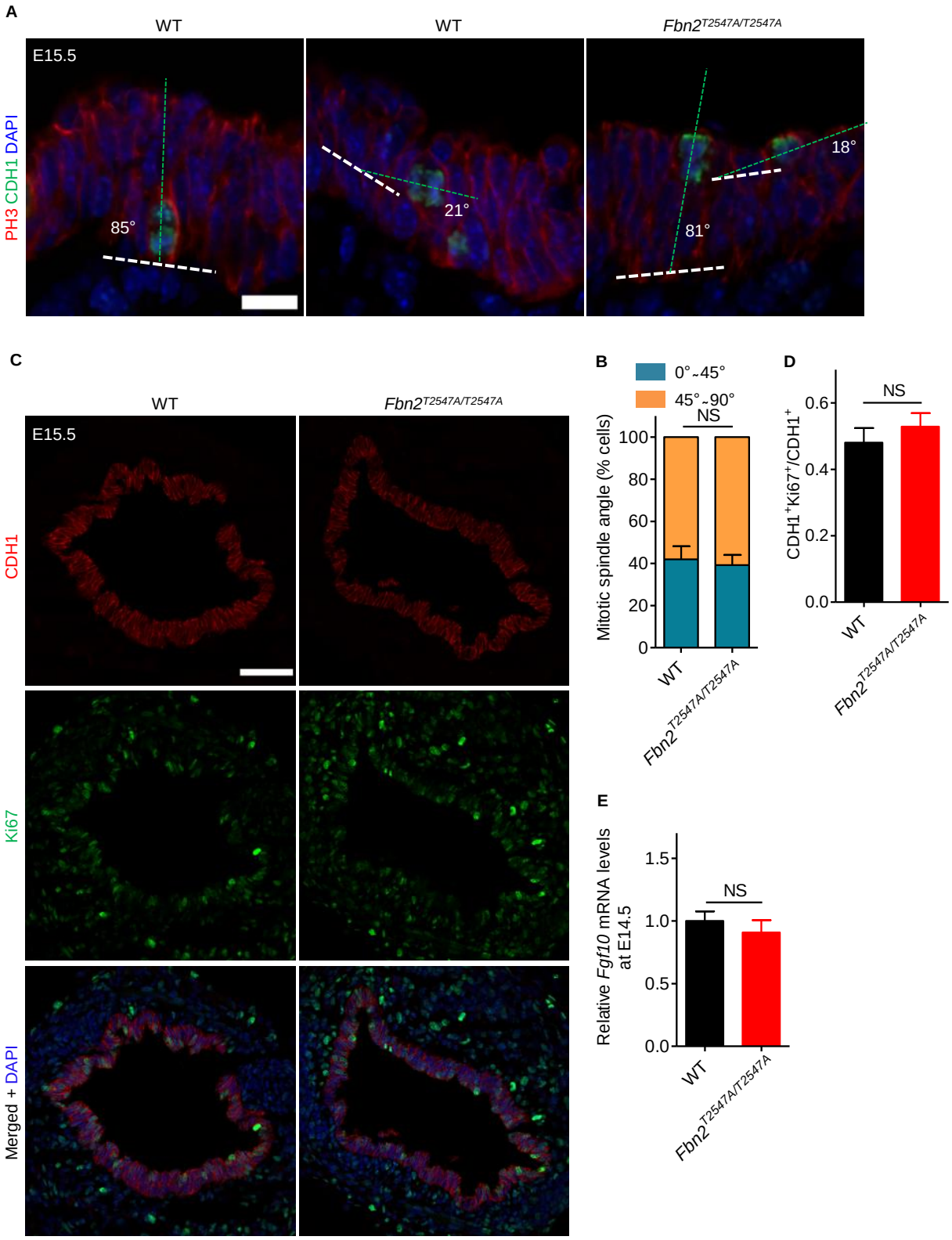
A
WT
WT
Fbn2T2547A/T2547A
E15.5
PH3 CDH1 DAPI
85°
21°
81°
18°
C
WT
Fbn2T2547A/T2547A
E15.5
CDH1
Ki67
Merged + DAPI
B
0°~45°
45°~90°
NS
Mitotic spindle angle (% cells)
100
80
60
40
20
0
WT
Fbn2T2547A/T2547A
D
NS
CDH1+Ki67+/CDH1+
0.6
0.4
0.2
0.0
WT
Fbn2T2547A/T2547A
E
NS
Relative Fgf10 mRNA levels at E14.5
1.5
1.0
0.5
0.0
WT
Fbn2T2547A/T2547A

Figure S13

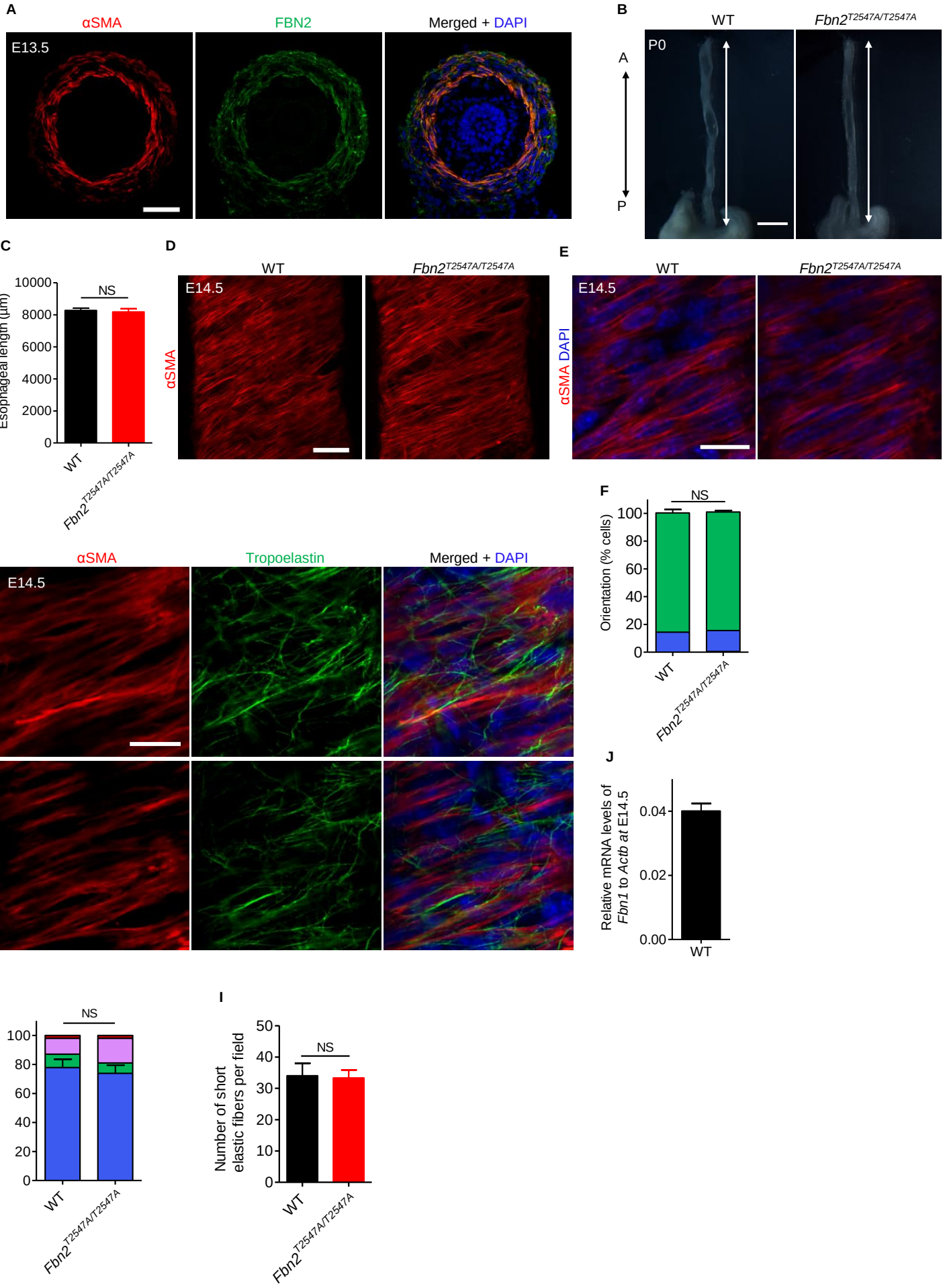
A
αSMA
FBN2
Merged + DAPI
E13.5
B
WT
Fbn2T2547A/T2547A
P0
A
P
C
NS
Esophageal length (µm)
10000
8000
6000
4000
2000
0
WT
Fbn2T2547A/T2547A
D
WT
Fbn2T2547A/T2547A
E14.5
αSMA
E
WT
Fbn2T2547A/T2547A
E14.5
αSMA DAPI
F
NS
Orientation (% cells)
100
80
60
40
20
0
WT
Fbn2T2547A/T2547A
G
αSMA
Tropoelastin
Merged + DAPI
E14.5
WT
Fbn2T2547A/T2547A
J
Relative mRNA levels of Fbn1 to Actb at E14.5
0.04
0.02
0.00
WT
H
NS
% elastic fiber orientation
100
80
60
40
20
0
WT
Fbn2T2547A/T2547A
I
NS
Number of short elastic fibers per field
50
40
30
20
10
0
WT
Fbn2T2547A/T2547A

Figure S14

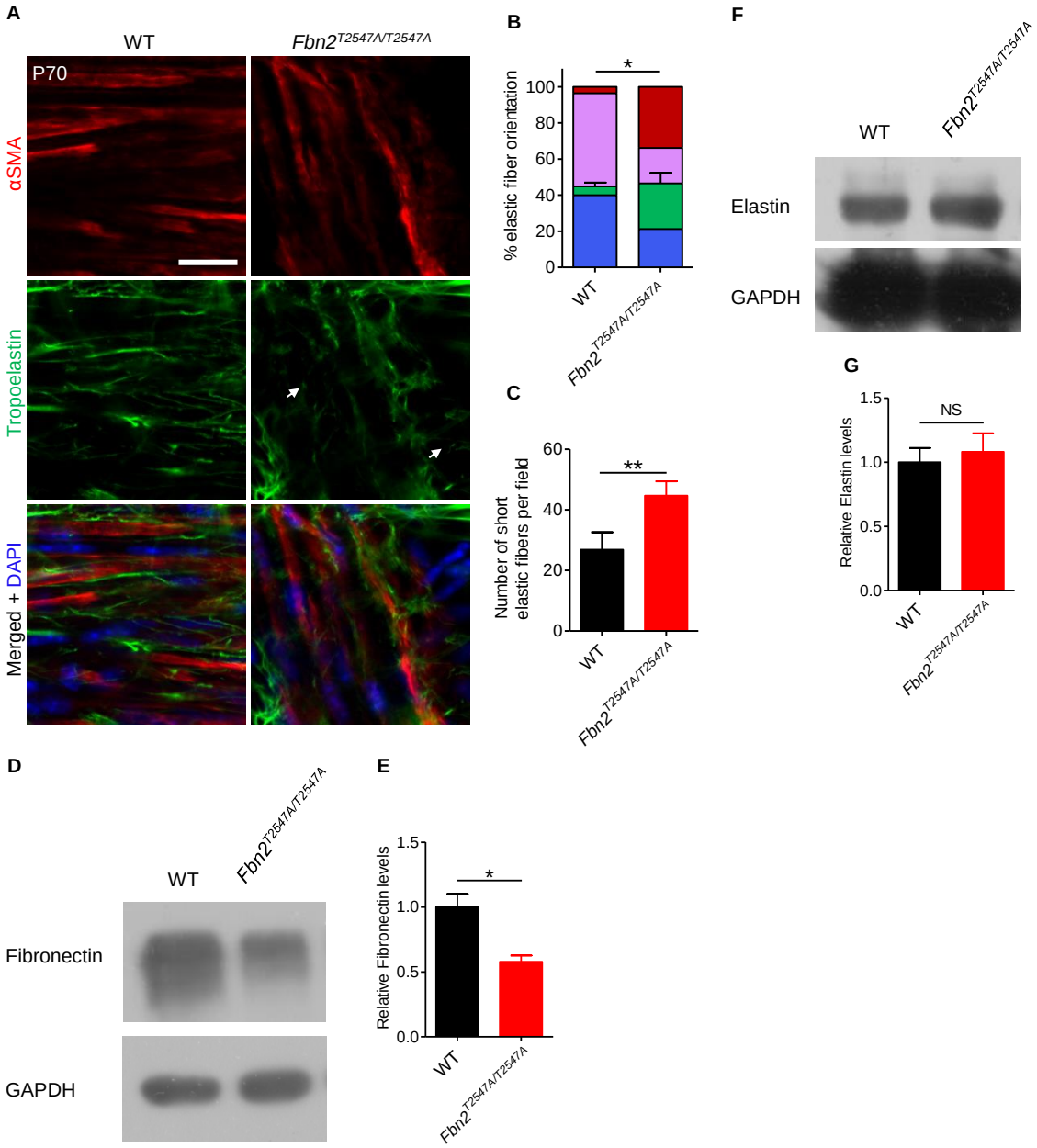
A
WT
Fbn2T2547A/T2547A
P70
αSMA
Tropoelastin
Merged + DAPI
B
% elastic fiber orientation
100
80
60
40
20
0
*
WT
Fbn2T2547A/T2547A
C
Number of short elastic fibers per field
60
40
20
0
**
WT
Fbn2T2547A/T2547A
F
WT
Fbn2T2547A/T2547A
Elastin
GAPDH
G
Relative Elastin levels
1.5
1.0
0.5
0.0
NS
WT
Fbn2T2547A/T2547A
D
WT
Fbn2T2547A/T2547A
Fibronectin
GAPDH
E
Relative Fibronectin levels
1.5
1.0
0.5
0.0
*
WT
Fbn2T2547A/T2547A

Figure S15

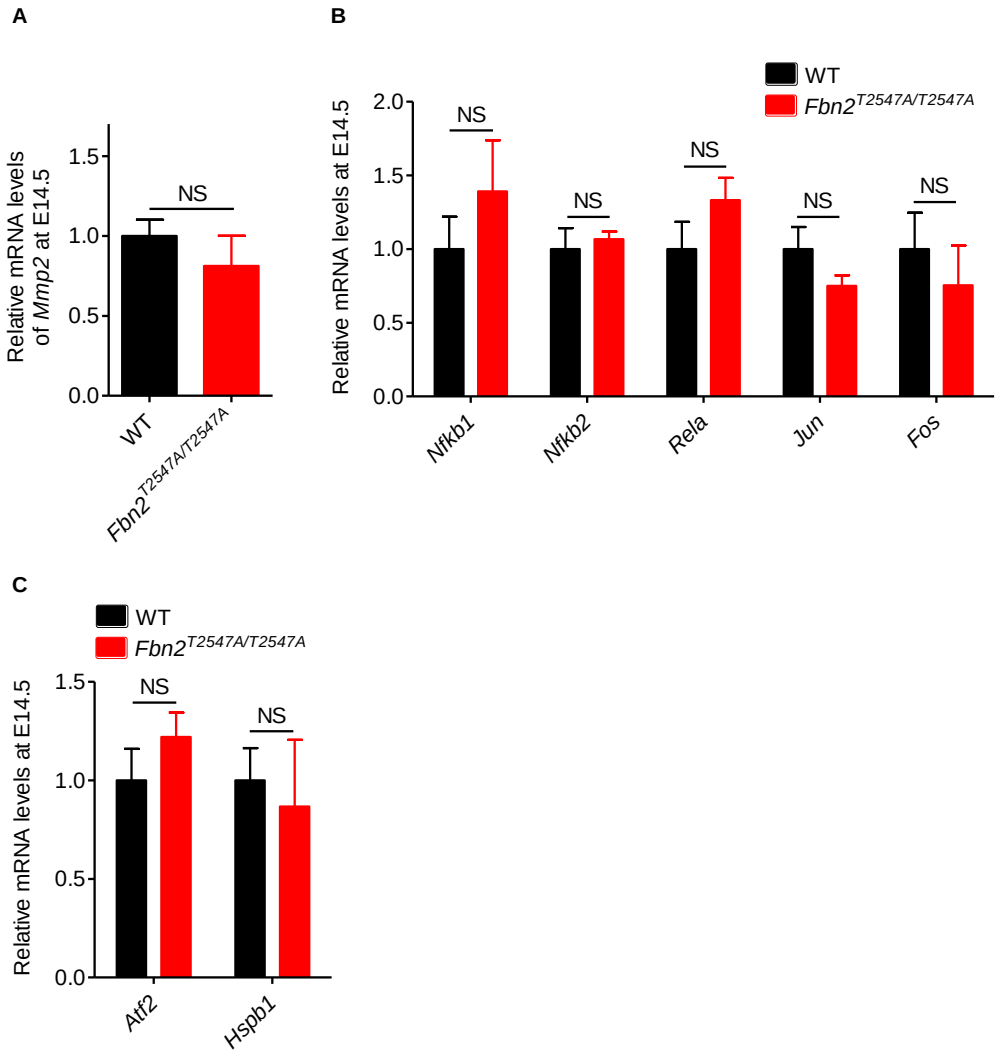
A
Relative mRNA levels of Mmp2 at E14.5
1.5
1.0
0.5
0.0
NS
WT
Fbn2T2547A/T2547A
B
Relative mRNA levels at E14.5
2.0
1.5
1.0
0.5
0.0
WT
Fbn2T2547A/T2547A
NS
NS
NS
NS
NS
Nfkb1
Nfkb2
Rela
Jun
Fos
C
WT
Fbn2T2547A/T2547A
Relative mRNA levels at E14.5
1.5
1.0
0.5
0.0
NS
NS
Atf2
Hspb1

Figure S16

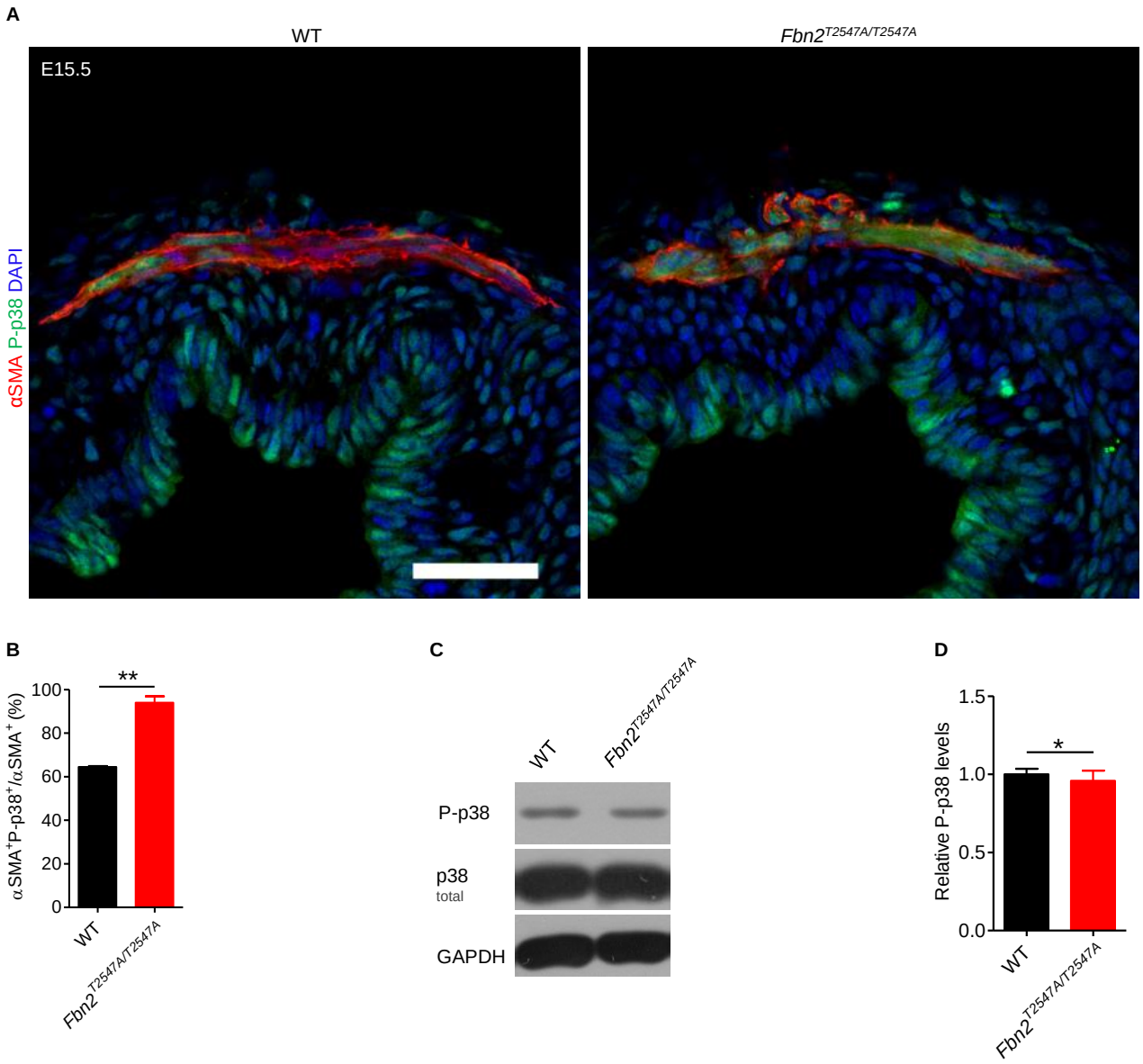
A
WT
Fbn2T2547A/T2547A
E15.5
αSMA P-p38 DAPI
B
αSMA+P-p38+/αSMA+ (%)
100
80
60
40
20
0
**
WT
Fbn2T2547A/T2547A
C
WT
Fbn2T2547A/T2547A
P-p38
p38
total
GAPDH
D
Relative P-p38 levels
1.5
1.0
0.5
0.0
*
WT
Fbn2T2547A/T2547A

Figure S17